CDF/ANAL/JET/CDFR/10841
Draft 1.6
May 8, 2014

Central Exclusive Production of Hadrons (Double Pomeron Exchange) in CDF

Artur Swiech, Maria Zurek
Jagiellonian University, Cracow, Poland

Michael Albrow, Jonathan Lewis
Fermi National Accelerator Laboratory, USA

Jon Wilson
University of Michigan, USA

Erik Brücken
University of Helsinki, Finland

Denys Lontkowsky, Inna Makarenko
University of Kiev, Ukraine

Abstract

We present a study in CDF of $p\bar{p}$ collisions at the Tevatron that have two charged hadrons in the central region, $|\eta| < 1.3$ with large rapidity gaps (no hadrons) on either side. The reaction is $p + \bar{p} \to p + X + \bar{p}$, where the "+" stands for a rapidity gap G; we use the notation GXG. Here we present a study of events with exactly two charged hadron tracks in the central detector, which we show to be often the result of the decay of a single neutral resonance, such as f_0^0 or f_2^0 states. These events are expected to be dominated by double pomeron, $\mathbb{P}$, exchange in the t-channel; hence $\mathbb{P}+\mathbb{P} \to X$. Only specific quantum numbers for X are allowed. Additionally, we see a signal for photoproduction of the J/ψ state, which provides a check of our mass scale, resolution, and cross section calculation. We also place limits on exclusive production of χ_{c0} production and decay in the $\pi^+\pi^-$ and K^+K^- channels.

We use data taken at $\sqrt{s} = 1960$ GeV and 900 GeV.

This data provides a useful window on hadron spectroscopy, as well as providing benchmarks for testing pomeron models.

Contents

1 Introduction

The pomeron, $\mathbb{P}$, can be defined as the carrier of 4-momentum between protons when they scatter elastically at high (i.e. collider) energies. It is therefore a strongly interacting color singlet state, at leading order a pair of gluons: $\mathbb{P}= gg$. Of course in QCD it cannot be a pure state, because quark pairs and other gluons must evolve in when Q^2, which we can equate with the 4-momentum transfer^2 t, becomes large. When Q^2 is small ($\lesssim$ 2 GeV^2) which is usually the case with pomeron exchange, perturbative QCD cannot be used to calculate cross sections, as the coupling $\alpha_s(Q^2)$ becomes of order 1. Non-perturbative methods, such as Regge theory, are more applicable [1, 2, 3]. It is a challenge to theorists to derive Regge theory from QCD, but after 40 years it has not happened. Meanwhile the subject is largely data-driven and phenomenological, hence the value of new data such as in this study.

It has been known since the days of the Intersecting Storage Rings, ISR, at CERN (pp with $\sqrt{s} = 23 - 63$ GeV) that one can have pp interactions with more than one pomeron, $\mathbb{P}$, exchanged, known as double pomeron exchange, D$\mathbb{P}$E. See [4] for a review. This process $\mathbb{P}+\mathbb{P} \to X$ allows an experimental approach to better understand the pomeron. One should not think of pomerons as isolated entities being emitted from the protons that then interact; the pomeron is only a t-channel exchange. In some (more perturbative) cases D$\mathbb{P}$E can also be thought of as $g + g \to X$ with another (soft) gluon(s) exchanged to cancel the color and allow the protons to (sometimes) emerge intact. This gluon fusion mechanism is clearly an excellent channel to produce glueballs, hadrons with no valence quarks. Sometimes the protons will dissociate into a low-mass state, e.g. $p \to p\pi^+\pi^-$. This is diffractive dissociation; it should not affect the properties of X. In CDF we cannot detect the outgoing protons, but we can select events with large rapidity gaps $\Delta y \gtrsim 4$ on each side of X. However the cross sections we measure will be larger than the fully exclusive process: $p+X+p$. Whether the protons stay intact or not, the central state will be dominated by D$\mathbb{P}$E. Photon exchanges are allowed, but the cross sections will be much smaller ($\gamma\gamma$ interactions are visible in exclusive lepton pair production since there is no D$\mathbb{P}$E contribution.)

When $M(X) \lesssim 3$ GeV/c^2 the main interest is for specific ("exclusive") states with well defined quantum numbers; when $M(X) \gtrsim 10$ GeV/c^2 the (multi-)partonic structure of the pomeron is probed, and one may find new phenomena related to the fact that it is *not* a hadron, but is nevertheless a strongly-interacting color singlet without valence quarks. High mass central states are the subject of a different study, not included in this note.

Investigation of these interactions will enhance our understanding of QCD in the non-perturbative regime. CDF is an excellent detector for this physics, and while the LHC detectors would be suitable, the running conditions are such that there are very few interactions with no pile-up, which is a necessary condition for this physics (unless one measures both leading protons, as in the PPS (Precision Proton Spectrometer, formerly HPS) projects). However LHC experiments are beginning to study these low mass exclusive hadron processes (there are no publications yet). In CDF we have a

much larger data sample. We also have data at both $\sqrt{s} = 900$ GeV and 1960 GeV, and the s-dependence is instructive.

This data may make a valuable contribution to meson spectroscopy. States with a large gluonic content ("glueballs" or hybrids) should be favored, in contrast to $\gamma\gamma \to X$ where $q\bar{q}$ states are favored.

In CDF we have previously published the *first observations* of several central exclusive production, CEP, processes in hadron-hadron collisions. We measured $\gamma + \gamma \to e^+e^-$ [5, 7] and $\mu^+\mu^-$ [6, 7], and photoproduction: $\gamma + \gamma \to J/\psi, \psi'(2S)$ and put the first upper limit on $\gamma + \mathbb{P} \to Z$. In $\mathbb{P}+\mathbb{P}$ interactions we measured an inclusive cross section with the $\bar{p}$ detected in Roman pots and a gap on the other side [8], we made the first observations of exclusive $\mathbb{P}+\mathbb{P} \to$ Jet + Jet [9] [112+ citations], χ_{c0} [6] [93+ citations], and, of great importance, $\gamma\gamma$ [10] [75+ citations]. Exclusive production of low mass hadronic states has a long history going back to the ISR, the SPS and the Tevatron (fixed target) [4]. However only at the top ISR energy, $\sqrt{s} = 63$ GeV, could one have rapidity gaps as large as $\Delta y = 3$ (a minimal requirement for pomeron exchange dominance over other Regge (π, ρ) exchanges on both sides of X). The ISR published data are for $\pi^+\pi^-$, and with small samples of K^+K^-, $\rho\rho$, and $p\bar{p}$ events.

2 Relevant CDF detectors

For the results in this study we used all the CDF detectors. Unless otherwise stated we assume all charged hadrons are pions, without using $\pi/K/p$ separation from dE/dx or Time-of-Flight. The former is only useful at very low momenta and the latter is of limited use in these 2-track events (it cannot distinguish $\pi^+\pi^-$ and K^+K^- events if the particles have the same path length *and* the same momenta). Later we will show that the K^+K^- background, when assuming both particles are pions, is $<$ a few %. The muon chambers are used only to reject for background stubs. We will select events with exactly 2 COT tracks, with $\sum Q = 0$. In addition, to understand the $K\bar{K}$ background, we have selected events with four tracks consistent with two $K^0_S \to \pi^+\pi^-$. We want to select events with no other hadrons produced, and we will require no other charged tracks and that all the calorimetry (except around the impact points of the charged particles), the BSC-1 counters, and the CLC have no signals above the noise levels.

This data was taken after the outer BSC counters (BSC-2 and BSC-3) and the MiniPlug were decommissioned. We are therefore blind to $|\eta| > 5.9$, and accept events where the proton was quasi-elastically scattered or where it dissociated (= fragmented) into a low mass state. We have data at both $\sqrt{s} = 900$ GeV and 1960 GeV; the beam proton rapidities are $y_{beam} = \ln(\sqrt{s}/m(p)) = 6.87$ and 7.64 respectively. The "rapidity space" available for proton dissociation products is approximately (mixing true and pseudo-rapidities) $\Delta y(diss) = y_{beam} - 5.9 \sim 1.0$ and 1.74 respectively. The higher dissociation masses allowed at 1960 GeV than at 900 GeV will contribute to a higher measured cross section, and affect the quantum number selection rules; this should be

borne in mind when studying the s-dependence of the cross sections.

2.1 Forward detectors for gap requirements

BSC-1, which covers $5.4 < |\eta| < 5.9$, was kept after BSC-2 and BSC-3 were decommissioned. We put BSC-1 in veto in the level 1 trigger. Each has four PMTs, one for each quadrant, and has 9.5 mm (1.7 X_0) of lead radiator in front to convert photons. The Cherenkov luminosity counters, CLC, were also put in veto. (These were not used in our earlier exclusive studies, which had the Miniplug covering the same angular region.) The CLC cover $3.75 < |\eta| < 4.75$ on each side, and each consists of 48 long gas-filled Cherenkov counters (with one PMT each). They are arranged in three concentric rings. With isobutane at 1.2 atm. one expects about 100 photoelectrons for a $\beta = 1$ particle along the axis. Signals are also observed with fewer photoelectrons, at least partly caused by showers in nearby material (plug, beam pipe, etc.).

BSC-1 and the CLC together cover from $|\eta| = 3.75$ to 5.9, and a gap $\Delta\eta = 2.15$ is not enough for pomeron dominance (Reggeon exchanges are still important). We therefore extend the veto region using the forward plug calorimeter, which covers $2.11 < |\eta| < 3.64$, at Level 2. The small "hole" between 3.64 and 3.75 is not very important, partly because of the "splash-out" detection by the CLC, and also because the chance of having no particles between 2.11 and 5.9 *except* in that hole is small, and will give a very small background. There is also a gap between the CLC and BSC1, $\eta = 4.75$ - 5.4. We were able to show from 0-bias data that the probability that an event satisfying the forward plug, CLC and BSC1 vetos, and therefore our trigger, has a hit in the small uncovered gap is only a few %, by simulating the trigger in 0-bias data taken when the Miniplugs were operational. Off-line we will require that the gaps extend through the plug regions to $|\eta| = 1.3$, so apart from the small cracks noted above we have wide gaps with $\Delta\eta > 4.6$.

3 Trigger and Data set

3.1 Trigger

The trigger used is: DIFF_TWO_CJET0.5_PLUGVETO_0.75

with the total luminosity for that trigger being 7.12/pb at 1960 GeV and 0.074/pb at 900 GeV

At level 1 we required no signal (above about 1 M.I.P.) in any of the BSC1 counters, with $5.4 < |\eta| < 5.9$. We also required no charged particles detected in the CLC with $3.75 < |\eta| < 4.75$. (We found that the CLC single particle signal drifted since installation and we needed to take that into account in luminosity normalization.) Together these gap requirements (on both East and West sides) veto a very large fraction of inelastic collisions, especially when there is more than one collision in the bunch crossing. We included at level 1 the positive requirement of at least two central ($|\eta| < 1.32$) calorimeter towers above a very low threshold, namely $E_T > 0.5$ GeV

(TWO CJET0.5). This is the jet trigger turned down as low as possible (above noise), and uses the sum of the EM and HAD energy in a trigger tower.

At level 2 we made the tighter gap requirement with a Plug Veto, with $2.11 < |\eta| < 3.64$. We required $\sum E_T < 0.75$ GeV on both E and W sides. We thus have a rapidity gap in the trigger of about 3.8 units on each side, apart from the small crack between CLC and BSC-1. For the offline analysis of events with only COT tracks the gaps are longer ($|\Delta\eta|$ = 1.3 - 5.9). It is well known that over such large gaps, to a very good approximation, only pomeron or photon exchange is allowed (whether or not the proton fragments), and as the photon coupling is only about 1% of the pomeron coupling, $\gamma\gamma$ exchange processes are relatively negligible in central hadron production.

3.2 Data sets

The data sets used are **gdifam** and **gdifap** at 1960 GeV (about 115 million triggered events) and **gdifar** at 900 GeV (about 22 million triggered events during s-scan). Data taken at $\sqrt{s}$ = 300 GeV, also with **gdifar**, have much lower statistics and relatively poor beam conditions, and we do not use it here.

4 Rapidity gap cuts, exclusive selection

In this section we explain the off-line selection of exclusive 2-track (h^+h^-) events. To understand the noise levels in all the detectors, we use zero-bias (bunch crossing) triggers, taken during the same periods. We did this independently for the 1960 GeV and 900 GeV runs. We divided the 0-bias data into two classes:

- (A) No interactions, defined as no tracks, no muon stubs, and no CLC hits,
- (B) all the other events, totally dominated by one or more inelastic interactions.

For each subdetector we compare the signals in the two classes, with (A) dominated by noise. In CDF we have previously successfully used this method in two ways. In the search for exclusive Z-boson and observation of high mass lepton pairs [7], we summed the signals (e.g. ADC counts) in each subdetector, and imposed cuts on the sums. In our observations of exclusive χ_c [6] and $\gamma\gamma$ [10] we did not sum, but plotted the hottest channel, e.g. the PMT with the highest signal, and required that to be less than a cut. The methods give similar results. (If one had a very noisy channel it could kill real events and lower our efficiency, unless we were to ignore such channels. However it would not affect the cross section, because we measure the exclusive efficiency as described below. But we did not have any dominant noisy channels, so it is not relevant.)

4.1 Forward gaps

To illustrate the forward gaps selection with the detectors in the trigger, Fig. 1 shows the distribution of the sum of the BSC-1 East and West ADC counts (4 PMTs) ($\log_{10}$

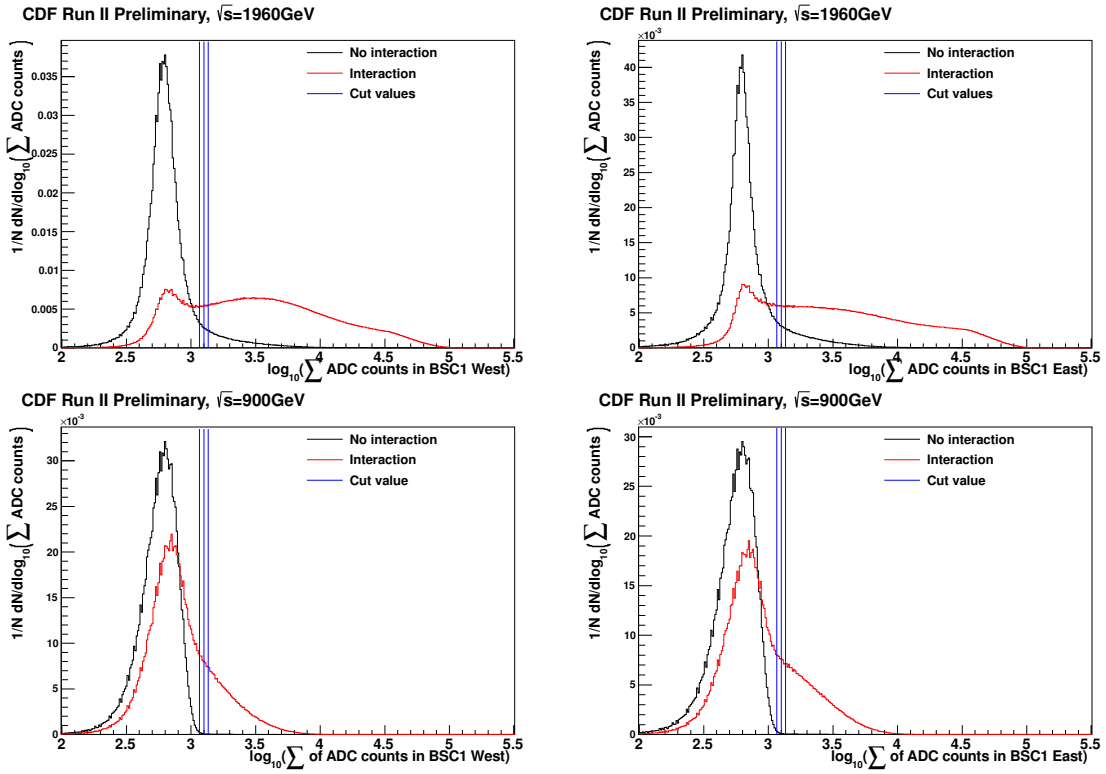

Figure 1: Interaction - No interaction separation in BSC1 West and East detectors determined for Zero-Bias data taken from same period as triggered data separately for $\sqrt{s} = 1960$ GeV and 900 GeV. Blue lines indicate cut value (middle) as well as loose and tight cut values used for systematic errors evaluation

scale) showing the noise-dominated and signal-dominated distributions (900 and 1960 GeV). The interaction data shows a component at the noise level, because of course a sizeable fraction of interaction events have a gap in this counter, which only covers 0.5 units of pseudorapidity. The cut values (and those for the other forward detectors) are shown in Table 1. For the triggered events, after having required BSC-1 and CLC in veto, the corresponding distribution is shown in Fig. 2, showing that the trigger is not cutting into the noise peak or allowing in signals, apart from a small tail. These are for the West and East side detectors; the plots are very similar, for all the sub-detectors, and similar cuts were made on both sides and at both (1960 GeV, 900 GeV) energies. The same discussion applies to the CLC plots, shown in Figs 3 and 4, and applies to the Forward Plug calorimeters, both EM and HAD (Figs. 5 and 7), showing the sum of energy in the plug regions. (Energy is more appropriate than E_T, since noise is independent of polar angle.) Table 1 lists the cut values applied to the forward detectors, and Table 2 shows the numbers of events after each exclusivity cut. These off-line cuts clean up and extend the forward gap requirement.

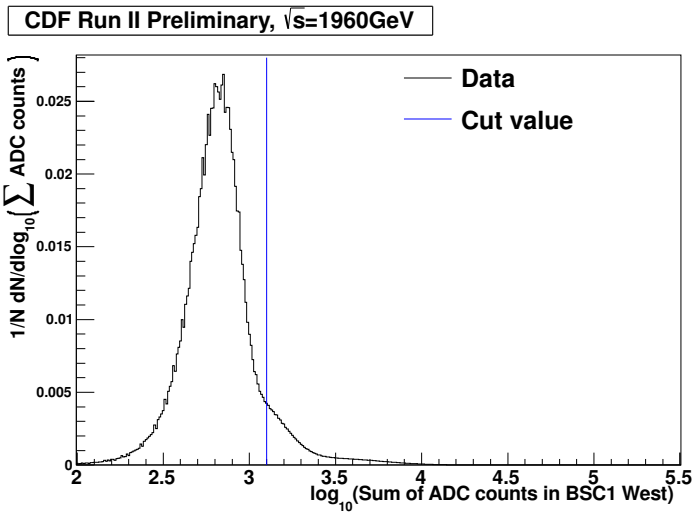

Figure 2: BSC-1 west signal for triggered data with blue line showing offline cut.

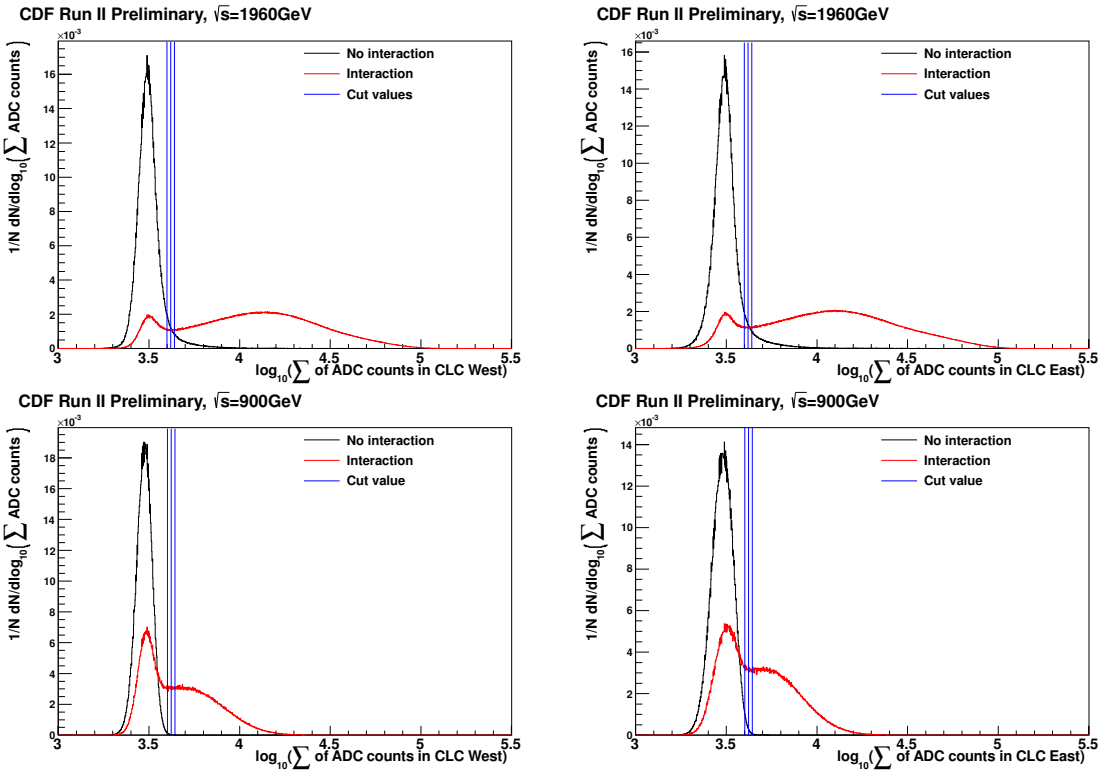

Figure 3: Interaction - No interaction separation in CLC West and East detectors determined for Zero-Bias data taken from same period as triggered data separately for 1960 GeV and 900 GeV $\sqrt{s}$ energies. Blue lines indicate cut value (middle) as well as loose and tight cut values used for systematic errors evaluation

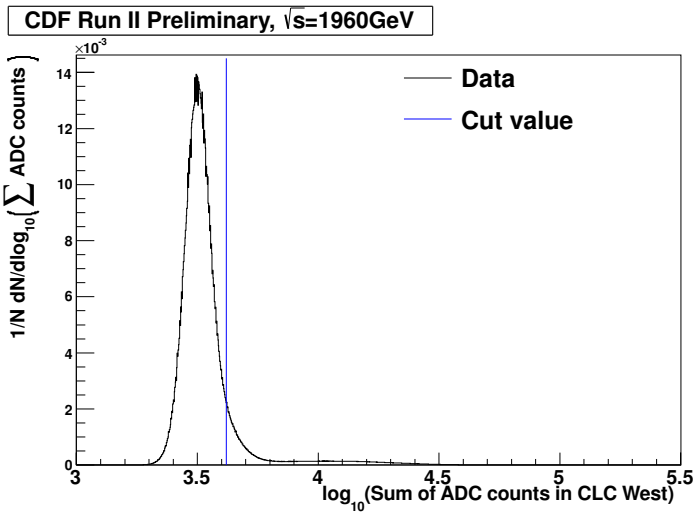

Figure 4: CLC west signal for triggered data with blue line showing the offline cut.

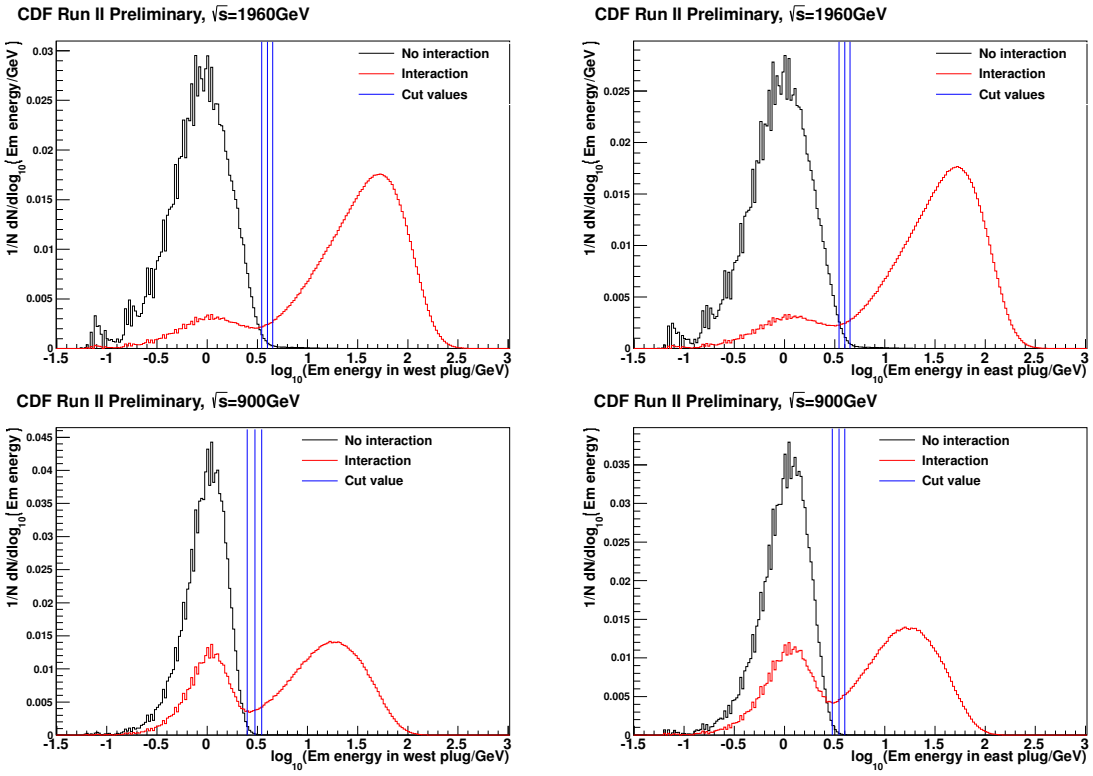

Figure 5: Interaction - No interaction separation in forward electromagnetic calorimeter west and east determined for Zero-Bias data taken from same period as triggered data separately for $\sqrt{s} = 1960$ GeV and 900 GeV. Blue lines indicate cut value (middle) as well as loose and tight cut values used for systematic errors evaluation

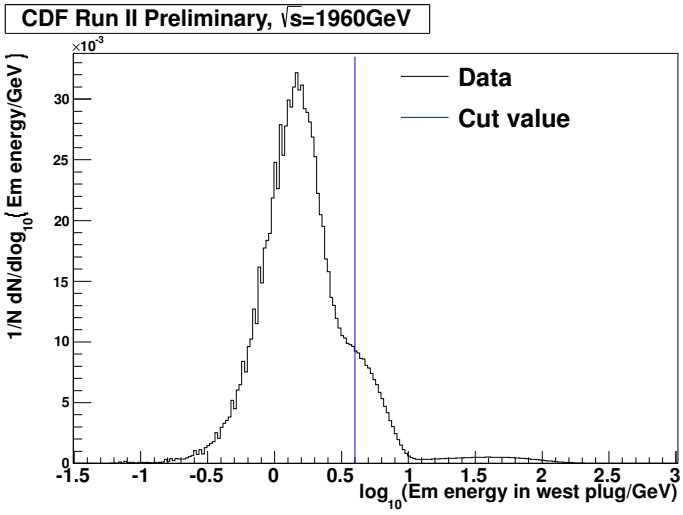

Figure 6: Energy in west forward electromagnetic calorimeter for triggered data with blue line showing the offline cut.

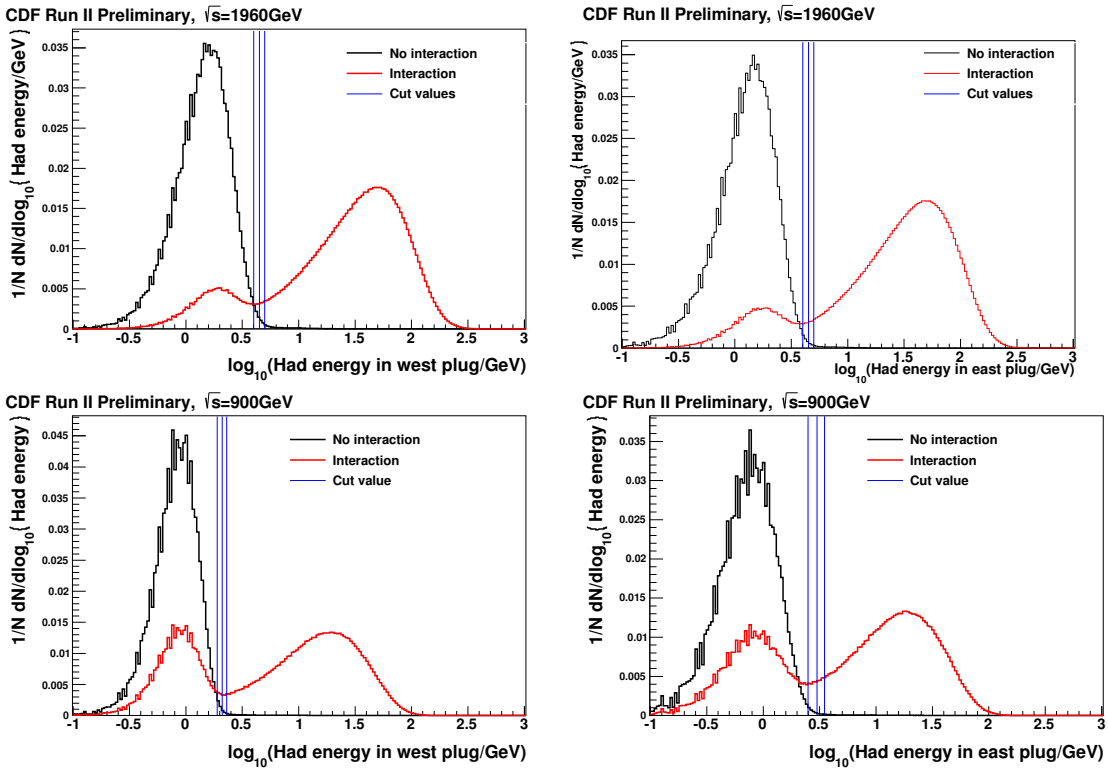

Figure 7: Interaction - No interaction separation in forward hadronic calorimeter west and east determined for Zero-Bias data taken from same period as triggered data separately for $\sqrt{s} = 1960$ GeV and 900 GeV. Blue lines indicate the cut value (middle) as well as loose and tight cut values used for systematic errors evaluation

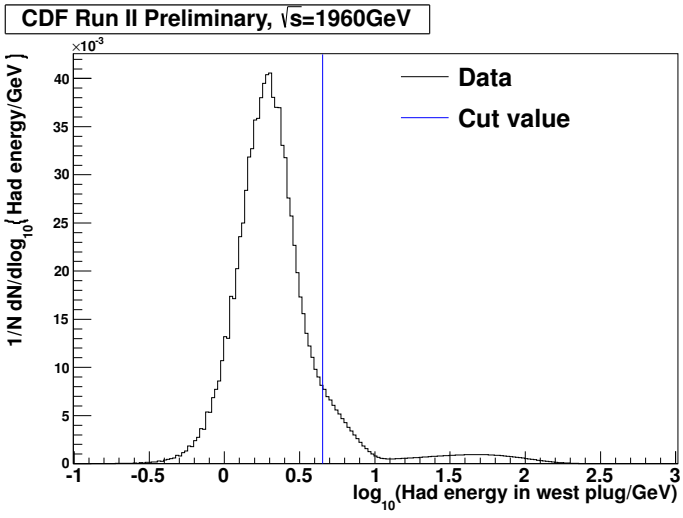

Figure 8: Energy in west forward hadronic calorimeter for triggered data with blue line showing offline cut.

Sub-detector	Cut at 1960 GeV	Cut at 900 GeV
$\sum$ ADC BSC-1 West	<1260 counts	<1260 counts
$\sum$ ADC BSC-1 East	<1260 counts	<1260 counts
$\sum$ ADC CLC West	<4170 counts	<4000 counts
$\sum$ ADC CLC East	<4170 counts	<4200 counts
$\sum$ E(EM) Plug West	<4.0 GeV	<3.0 GeV
$\sum$ E(EM) Plug East	<4.0 GeV	<3.5 GeV
$\sum$ E(HAD) Plug West	<4.5 GeV	<2.1 GeV
$\sum$ E(HAD) Plug East	<4.5 GeV	<3.0 GeV
$\sum$ E Central Calorimiters	<2.8 GeV	<0.8 GeV
Max E_t(EM) Central Calorimiters	<0.09 GeV	<0.08 GeV

Table 1: Cut levels for forward sub-detectors, to select only noise.

	1960 GeV	900 GeV
All triggered events	90230280	21736962
After BSC-1 clean up	82452800	21221532
After CLC clean up	82090232	21190520
After Fwd Plug EM cut	65303416	19778308
After Fwd Plug HAD cut	59538628	18749052

Table 2: Numbers of events after forward noise cuts.

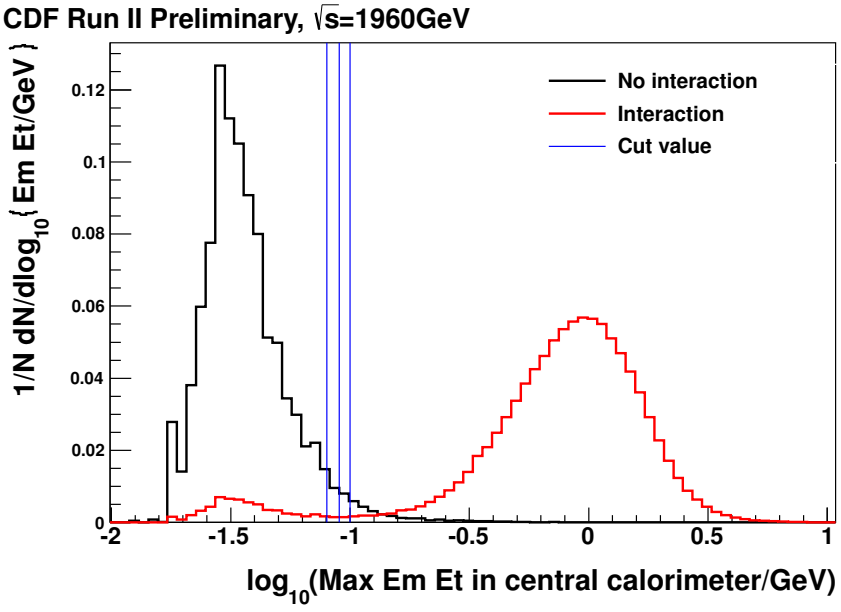

Figure 9: Interaction - No interaction separation based on the electromagnetic transverse energy of the hottest tower in Central Calorimeter detector determined for Zero-Bias data taken from same period as triggered data. Blue lines indicate cut value (middle) as well as loose and tight cut values used for systematic errors evaluation. $\sqrt{s}$ = 1960 GeV.

4.2 Central region exclusivity

After the forward exclusivity requirements, we now require that the central detectors are also at the noise level, except for the two charged tracks. The tracks are extrapolated to the calorimeters, and allowing for any energy in a cone of radius $\sqrt{\Delta\eta^2 + \Delta\phi^2} < 0.3$ around the hottest tower in 3x3 box around the extrapolated impact points. To addition to the procedure as for the forward detectors we apply additionaly cut on the emectromagnetic transverse energy E_t of the hottest tower outside the cones. Figs. 9 and 10 show the ($\log_{10}$) of the EM transverse energy of a hottest tower in the central calorimeters. Figs. 11 and 12 show the ($\log_{10}$) energy in the central calorimeters, in which the noise level is significantly lower at $\sqrt{s}$ = 900 GeV. A possible explanation is that at 1960 GeV there are 36×36 bunches, while at 900 GeV there are only 3×3, so the time between bunch crossings is 12× longer, and the noise levels decay. We used a different cut for the central calorimeter noise at the two energies, but all other detectors have the same cuts.

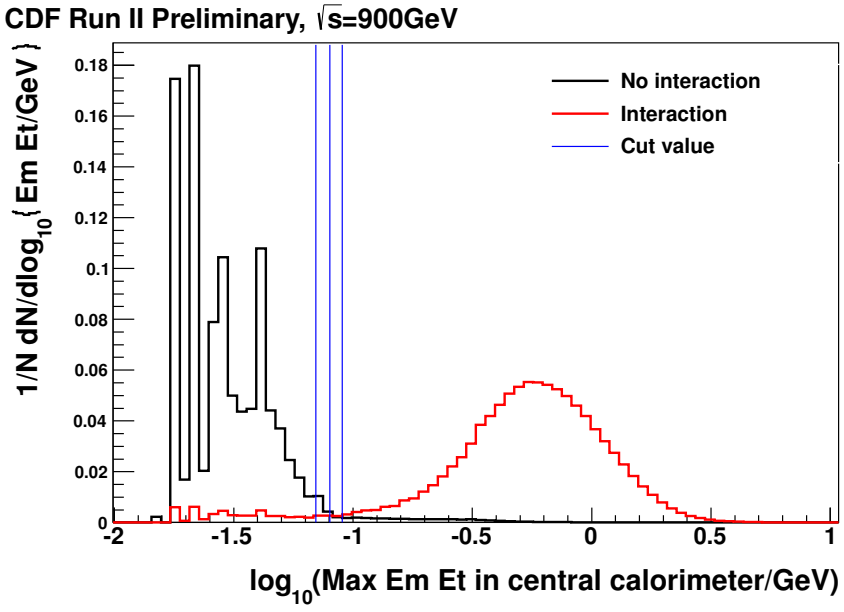

Figure 10: Interaction - No interaction separation based on the electromagnetic transverse energy of the hottest tower in Central Calorimeter detector determined for Zero-Bias data taken from same period as triggered data. Blue lines indicate cut value (middle) as well as loose and tight cut values used for systematic errors evaluation. $\sqrt{s}$ = 900 GeV.

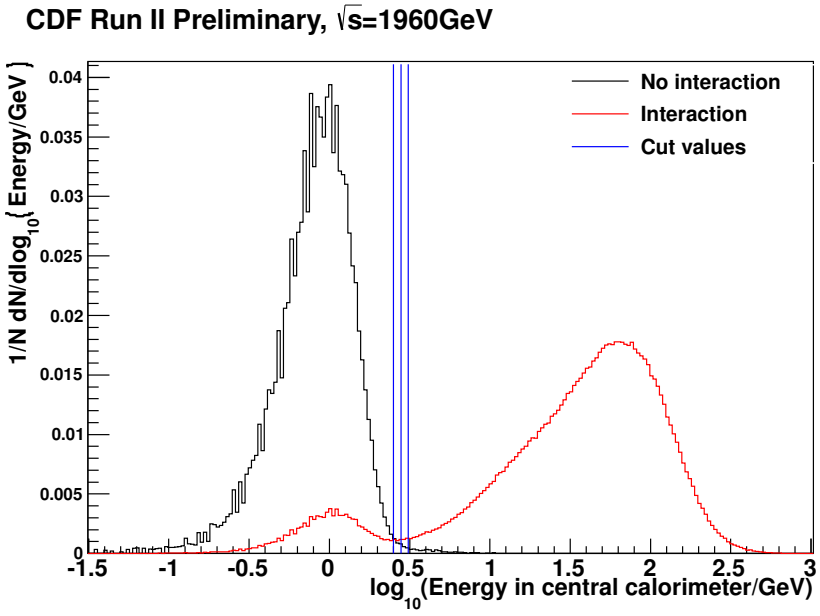

Figure 11: Interaction - No interaction separation based on a sum of energy in Central Calorimeter detector determined for Zero-Bias data taken from same period as triggered data. Blue lines indicate cut value (middle) as well as loose and tight cut values used for systematic errors evaluation. $\sqrt{s}$ = 1960 GeV.

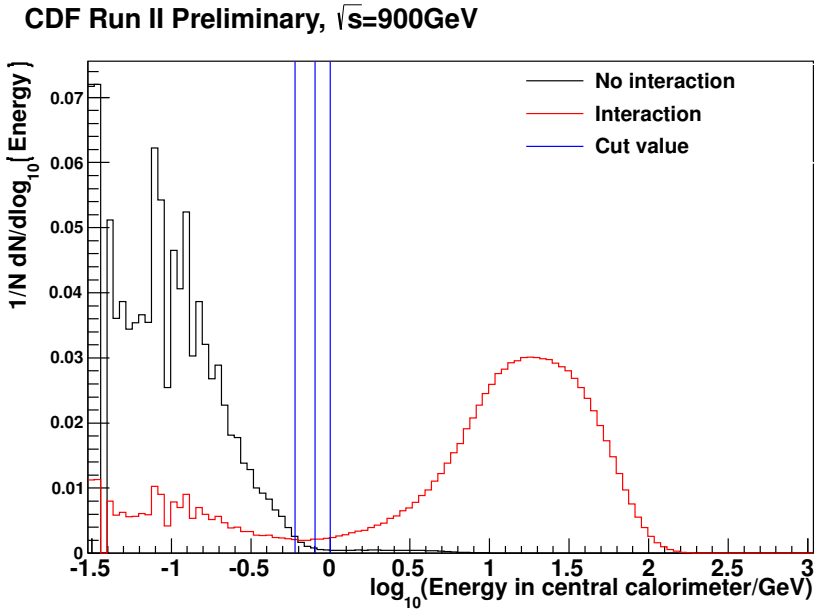

Figure 12: Interaction - No interaction separation based on a sum of energy in Central Calorimeter detector determined for Zero-Bias data taken from same period as triggered data. Blue lines indicate cut value (middle) as well as loose and tight cut values used for systematic errors evaluation. $\sqrt{s} = 900$ GeV.

5 Luminosity, exclusive efficiency, and effective luminosity

The luminosity $L(t)$ is normally given as $cm^{-2}s^{-1}$, integrating over all 36 bunches. But there are variations between the bunches, and as we need to know the probabilities of "no-pile-up" to get the exclusive efficiency, we use a different value, L_{bunch}, for each of the 36 bunches. (So $L(t) \sim 36 \times L_{bunch}$.) Pile-up depends on the luminosity for a *single* bunch-crossing, which is $L_{bunch}/47747$ (the number of orbits per second).

The bunch-by-bunch luminosities at $\sqrt{s} = 1960$ GeV are known in the standard way using the CLC counters. These detect a fraction $f(CLC)$ of the total inelastic cross section $\sigma(inel)$, and that fraction was determined from 0-bias events with low pile-up that had some energy above a threshold in the forward Plug calorimeter or ADC counts above threshold in the CLC counters [13]. The thresholds were varied, choosing either $E(Plug) > 3GeV, CLC-ADC > 250$ or $E(Plug) > 5GeV, CLC-ADC > 100$ as two options for cuts with good noise-signal separation, and the fraction of $\sigma(inel)$ detected is 0.95 for E OR W, and 0.78 for E AND W, using PYTHIA and MBR simulations.

During the $\sqrt{s} = 900$ GeV data-taking, knowing that the CLC luminosity calibration would be different, a quick estimate of the different cross section was made [14] and the constant was changed. However $f(CLC)$ was not known and so was not changed, the exact "before and after" values are at present unclear (and there was even some

doubt on-shift about the direction of the change!). Fortunately there is another method of calibrating the total luminosity, which we have tested with the 1960 GeV data, it agrees with the standard CLC method, and we can apply it to the 900 GeV data. So at 900 GeV the CLC are used for relative (time-dependent) luminosity monitoring, but not for cross sections.

The probability of an empty detector, $P(0)$, over $-5.9 < |\eta| < +5.9$ and using all the previously defined noise cuts, is measured as a function of the individual bunch×bunch luminosity times a correction factor: $K \cdot L_{bunch}$, where L_{bunch} is the value written in the data. K is *a priori* unknown, but we can find it from 0-bias data. We have $P(0) = e^{-\bar{n}} = e^{-\sigma(vis)\cdot K \cdot L_{bunch}/f_O}$, where $\bar{n}$ is the mean number of visible collisions (in $|\eta| < 5.9$) with cross section $\sigma(vis) = f(vis) \times \sigma(inel)$, and f_O is the orbit frequency, 47,747 s^{-1}. Knowing $\sigma(inel)$ from fits to total, elastic and therefore inelastic cross sections [15], and using event generators MBR, PYTHIA etc. to estimate $f(vis)$, we use the measured slope of $P(0)$ vs $K \cdot L_{bunch}$ to determine the correction K. Simply stated, we are using the whole detector instead of just the CLC to calibrate the luminosity, and we know $\sigma(vis)$ better than $\sigma(CLC)$, at least at 900 GeV.

$P(0)$ (also called ε_{exc}) is plotted vs. L_{bunch} for the two energies in Figs. 13 and 14. The distributions are good exponentials except at the highest 900 GeV bunch luminosities, where there are very few events. That tail corresponds to the first few minutes of the stores when beam conditions were bad. The exponential fit should extrapolate to 1.0 at $L_{bunch} = 0$, and it is 0.977±0.012 at 1960 GeV and 0.9928±0.0015 at 900 GeV. meaning that there is essentially no noise above the cuts that would give a non-empty detector even with no luminosity. Note that L_{bunch} is in $cm^{-2}s^{-1}$ and should be divided by the orbit frequency (47,747 s^{-1}) to get the *single* bunch crossing luminosity; $\bar{n} = \sigma(vis) \cdot K \cdot L_{bunch}/47,747$. Table 3 gives relevant values. The inelastic cross section values are taken from a global fit to $\sigma(tot)$ and $\sigma(elastic)$ including LHC 7 TeV data. The MBR estimate (Mary Convery, 05.10.12) is 53.8 mb and 61.8 mb respectively.

We see from Table 1 that the method of calibrating the luminosity by $\sigma(vis)$ agrees with the standard CLC-based method at $\sqrt{s} = 1960$ GeV within 4%, giving confidence that it can be used at 900 GeV.

$\sqrt{s}$ (GeV)	900	1960
$\sigma(inel)$ (TOTEM fit) (mb)	52.7±1.6	61.0±1.8
$f(vis)$ (MBR)	0.90±0.05	0.85±0.05
$\sigma(vis)$ (mb)	47.4±3.0	51.8±3.4
Uncorrected slope (mb)	65.79±0.38	55.88±0.13
K, change to luminosity ×	0.720±0.046	0.927±0.061
K^{-1}, change to cross sections ×	1.388±0.088	1.079±0.071

Table 3: Luminosity values at $\sqrt{s} = 900$ and 1960 GeV.

Adopting this method, the previous (CLC-based) cross sections plotted at 900 GeV

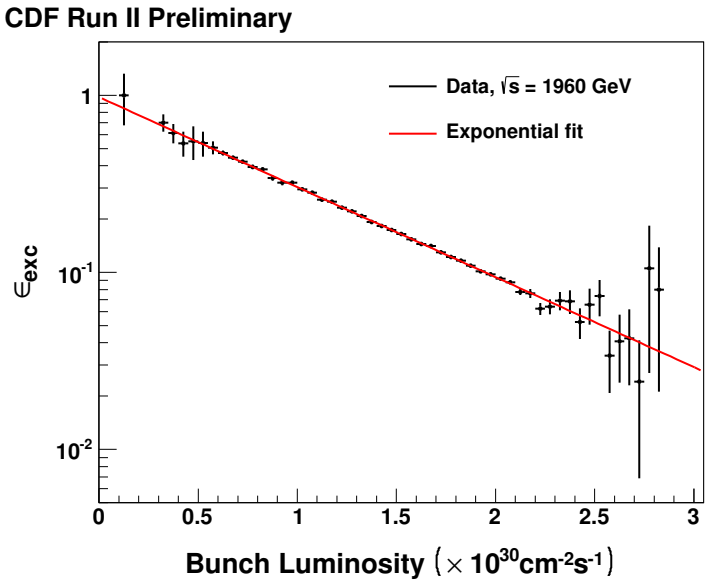

Figure 13: Exclusive efficiency as a function of bunch luminosity (from the CLC) for $\sqrt{s}$ =1960 GeV. The red line shows the exponential fit. The luminosity for a single bunch crossing is 47,747 times smaller than that plotted on the$x$-axis.

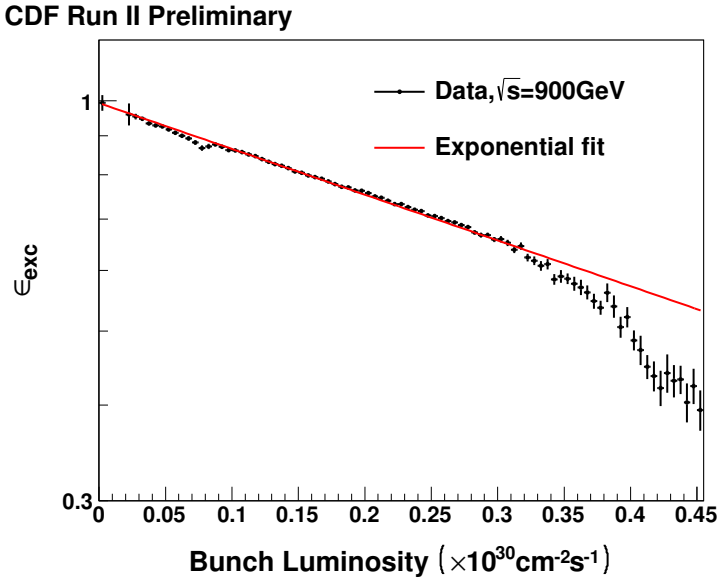

Figure 14: Exclusive efficiency as a function of L_{bunch} (from the CLC) for $\sqrt{s}$ =900 GeV. The luminosity for a single bunch crossing is 47,747 times smaller than that plotted on the$x$-axis. The calibrated (by $\sigma(vis)$) luminosity is smaller by a factor $K(\sim 30\%)$ than this CLC luminosity. The red line shows the exponential fit. The "sagging" at high bunch luminosity is caused by bad conditions (noise) at the beginning of the store.

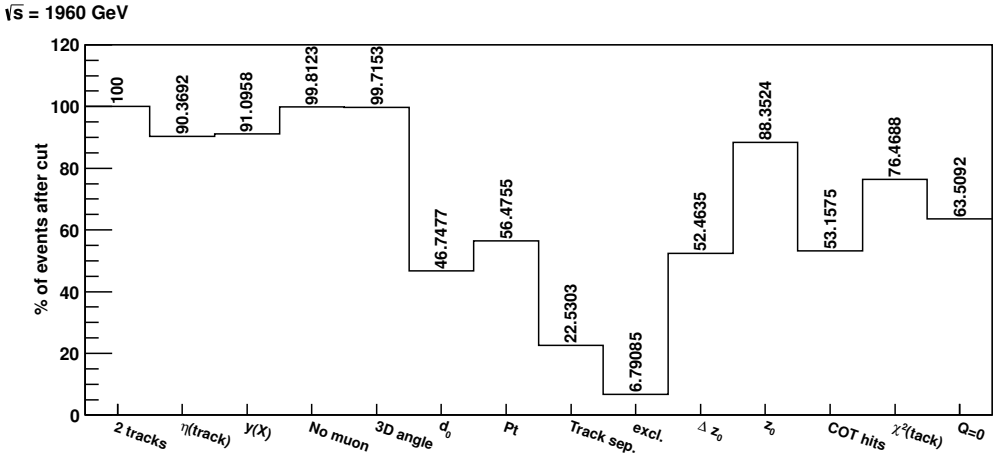

Figure 15: Percentage fraction of events remaining after particular cut for 1960 GeV data.

should be all be increased by a factor 1.31. The exclusive efficiency, $\varepsilon(excl)$ is the fraction of 0-bias events that pass all the noise cuts; it is equal to the probability that an event is not spoiled by another collision in the same bunch crossing. It is obtained from the distribution of $P(0)$ in 0-bias data weighted by the distribution of candidate events in the same data taking period, see Figs. 13 and 14. The exclusive efficiency does not change with $K \neq 1.0$; it is effectively a scale factor on the horizontal axis.

6 Two exclusive tracks; track quality cuts

The selection of 2-track events is made with a sequence of cuts, resulting in the numbers shown in Fig. 15 and 16. We give higher priority to having a clean, well measured, sample than to efficiency. A big reduction (30% survive the cut) comes from the central exclusivity requirement. A large part of that probably comes from events with two charged tracks + neutrals (especially π^0), which are of course expected.

We use the higher statistics 1960 GeV data to define the track cuts, and apply the same cuts at 900 GeV. Fig. 17 shows the η distribution of tracks. We define the central region (i.e. region for reconstructed tracks) to be in $|\eta| < 1.3$, where the trigger was active. The opening angle cut, Fig. 18, as well as the requirement of zero muons, eliminate the small background from cosmic ray tracks with $\theta_{3D} = \pi$. The track quality cuts consists of:

- Impact parameter to the nominal beam line cut, $d_0 < 0.1$ mm, (Fig. 19)
- The difference in z projected to the beam line $|dz_0| < 1.0$ cm, (Fig. 20)
- The number of COT hits in axial layers $\geqq 25$, (Fig. 21)
- The number of COT hits in stereo layers $\geqq 25$, (Fig. 22)

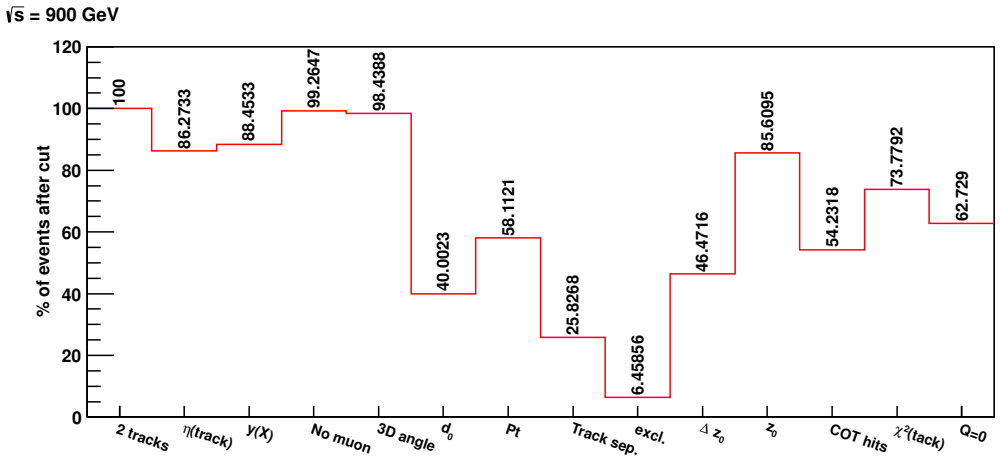

Figure 16: Percentage fraction of events remaining after particular cut for 900 GeV data.

- χ^2/DoF < 2.5 (Fig. 23)

To have a well-defined fiducial region and avoid rapidly changing thresholds we require both tracks to have $P_t > 0.4$ GeV/c, see Fig. 24. Additionally to be able to calculate the proper acceptance, we require that extrapolated tracks match two of the trigger towers with ± 1 tolerance in $iEta$ and $iPhi$, and the rapidity of the two-track state to be $|y(\pi^+\pi^-)| < 1.0$. Finally we require the tracks to have opposite charge. The numbers of (++) and (- -) pairs are similar. (The Q = 2 events presumably arise from 4-track events with two tracks outside the fiducial region and not giving big enough signals to be rejected by the exclusivity cuts.)

Table 4 shows the numbers of events at several stages of the analysis, and the effective luminosity, at the two $\sqrt{s}$-values. The events with two same charge tracks are 6.1% and 7.1% at 900 GeV and 1960 GeV respectively. They are an indication of non-exclusive background, probably 4-track events with two missed tracks, either below the p_T-threshold, in a calorimeter crack or very forward. We show them in Fig. 36. We expect there to be a similar number of Q = 0 events with missed tracks, but we do not subtract them as there is no reason for the mass spectra to be the same as the Q = 2 events.

6.1 Raw data mass distributions

We first show numbers of events and some features uncorrected for acceptance, and then we will describe the acceptance as a function of $M(\pi\pi)$ and $P_t(\pi\pi)$ and calculate cross sections. At both $\sqrt{s} = 900$ GeV and 1960 GeV, with the data selection $|\eta(\pi)| < 1.3, P_t(\pi) > 0.4$GeV/c, and $|y(\pi\pi)| < 1.0$, and no other particles in $|\eta| < 5.9$, the acceptance is the same apart from a small difference in the distribution of the interactions in z (the 900 GeV data did not have low-β and the region is longer).

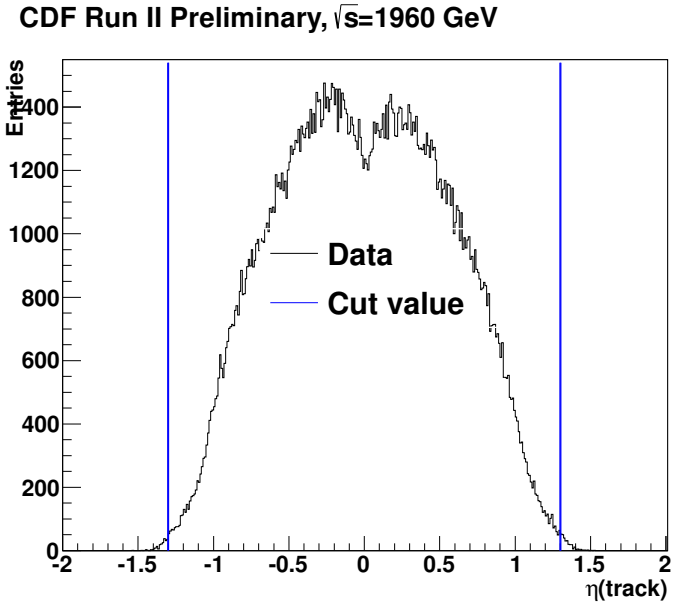

Figure 17: η distribution of tracks with cut and loose/tight versions, shown as blue lines.

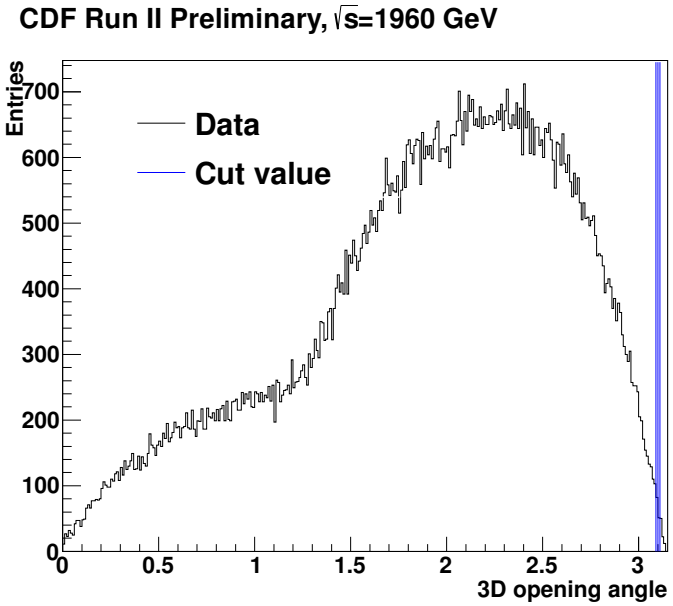

Figure 18: 3D opening angle distribution with cut and loose/tight versions, shown as blue lines.

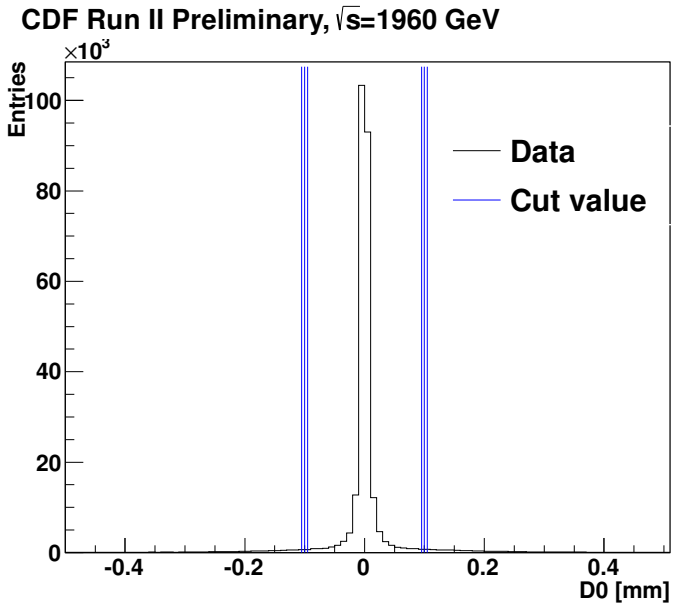

Figure 19: Impact parameter distribution with cut and loose/tight versions, shown as blue lines.

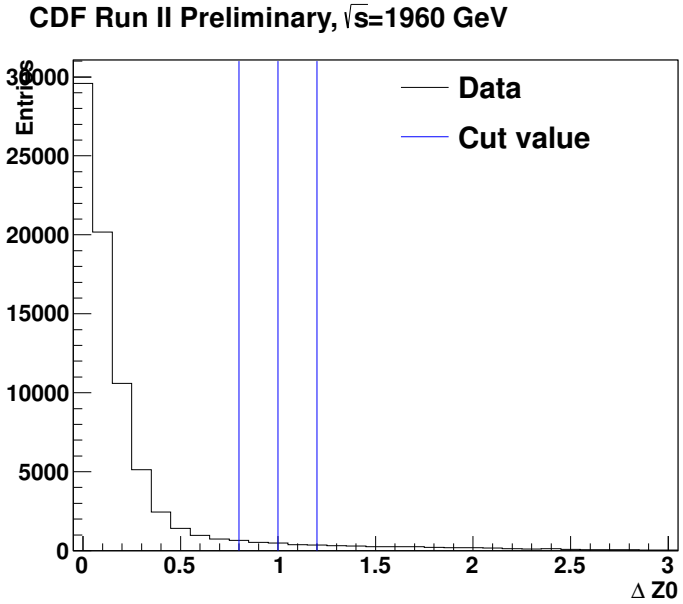

Figure 20: $|\Delta z_0|$ distribution with cut and loose/tight versions, shown as blue lines.

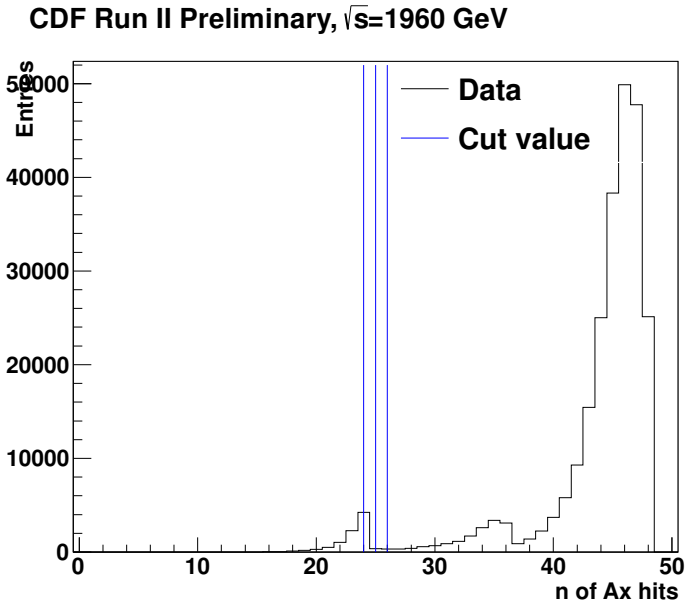

Figure 21: Distribution of number of hits in axial layers in COT with cut and loose/tight versions, shown as blue lines.

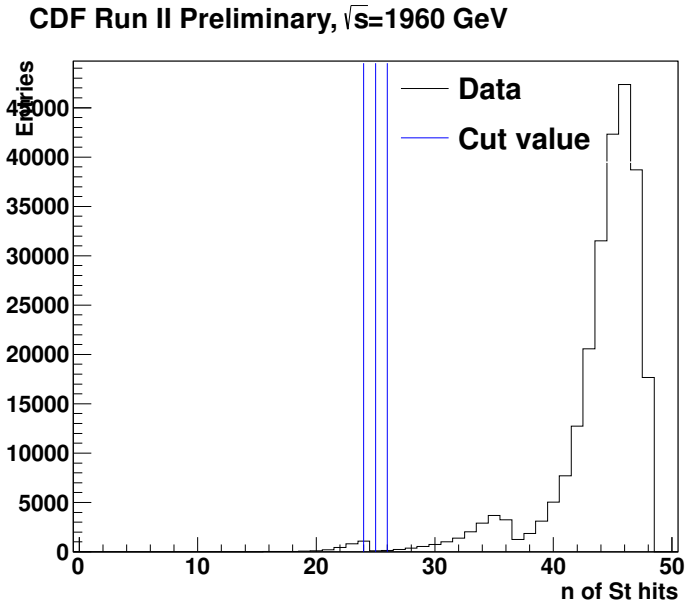

Figure 22: Distribution of number of hits in stereo layers in COT with cut and loose/tight versions, shown as blue lines.

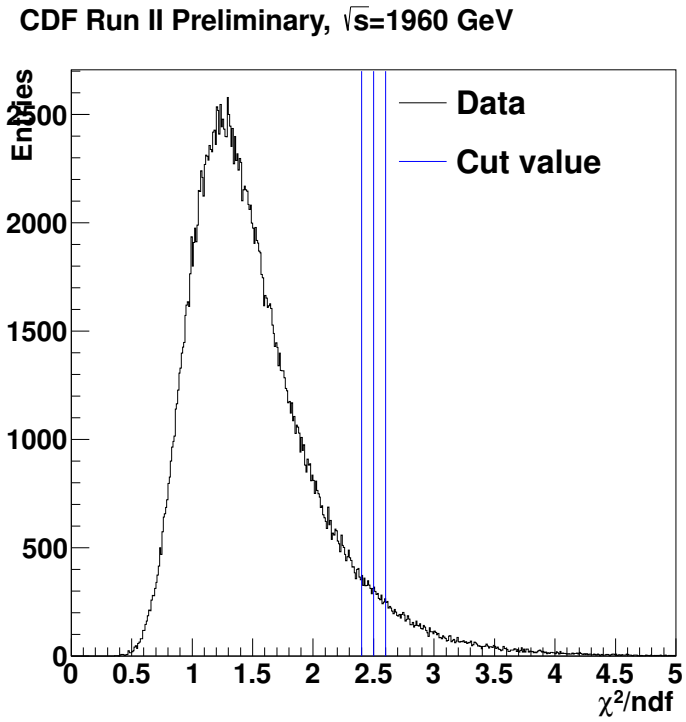

Figure 23: Distribution of χ^2 per degree of freedom of track fit.

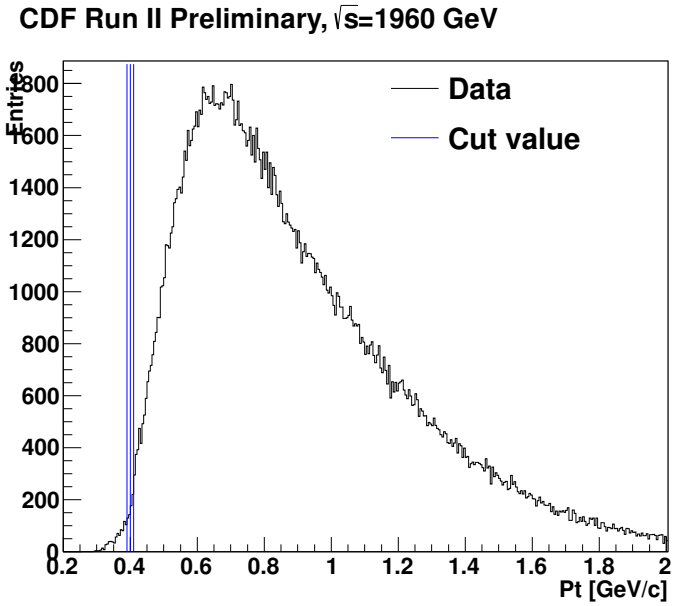

Figure 24: Distribution of track P_t with cut and loose/tight versions, shown as blue lines.

$\sqrt{s}$ =	1960 GeV	900 GeV
Triggered events	90230×10^3	21737×10^3
After Forward exclusivity cuts	59538×10^3	18749×10^3
Exactly 2 tracks	4721×10^3	271×10^3
Quality, exclusivity, cosmic rejection	137128	6646
Opposite sign	127340	6240
Luminosity	7.23 pb^{-1}	0.075 pb^{-1}
Exclusive efficiency	0.159	0.784
Effective (no-PU) luminosity	1.16 pb^{-1}	0.0590 pb^{-1}

Table 4: Numbers of 2-track events after sequential requirements.

So differences in the shape of the mass distributions should be not detector effects but physics, presumably mainly differences in allowed dissociation masses, together with some real $\sqrt{s}$-dependence of the DIPE cross sections. Even before correcting for acceptance we can note several qualitative features of the data.

Fig. 25 and Fig. 26 show the mass distributions of the events for two different $\sqrt{s}$, for all P_t, with statistical errors only, assuming that h^+h^- is $\pi^+\pi^-$. Above 5 GeV/c^2 there are only a few events. At both energies there is a large asymmetric peak between $1.0 < M(\pi\pi) < 1.5$ GeV/c^2, in the region of the $f_2(1270)$ and $f_0(1370)$ mesons. Table 5 shows all the states in the P.D.G. [16] with allowed quantum numbers: $I^GJ^{PC} = 0^+(even)^{++}$. There are some higher broad states, mostly not well established. Later we discuss a partial wave analysis (PWA) of the data. Other features visible in Fig. 25, thanks to its high statistics are (a) a peak just below 1 GeV/c^2, attributed to the $f_0(980)$ (b) an abrupt change of slope (almost a dip) at 1.5 GeV/c^2 (c) possible "ripples" between 1.5 and 2.5 GeV/c^2 (the acceptance in this region must at least be smooth) (d) at 3.1 GeV/c^2 there is a small peak atrributed (in Section 11) to photoproduction of the $J/\psi \to \ell^+\ell^-$ (we did not accept events with muon stubs, but muons from low-P_t J/ψ can range out in the calorimeters, and $J/\psi \to e^+e^-$ decays will be included).

Fig. 27 shows the ratio of raw data candidates at the two $\sqrt{s}$ values. The most obvious feature is a drop between 1.0 and 1.2 GeV/c^2 (after being constant from threshold to 1.0 GeV/c^2), possible structures between 1.5 and 2.0 GeV/c^2, and a gradual decrease from 2.0 to 5.0 GeV/c^2.

6.2 Comments on features and allowed meson states

The rise up to 1 GeV/c^2 in Fig. 25 is expected due to the the increasing acceptance at small P_t, as will be shown later, but the peak at 980 MeV is the $f_0(980)$ state. Table 5 shows a list of known (not all established) resonances that are allowed, by quantum numbers, to be produced exclusively in DIPE. They have $I^GJ^{PC} = 0^+\text{even}^{++}$. We see no signs of the $\rho(770)$, width = 150 MeV, which can be produced by exclusive

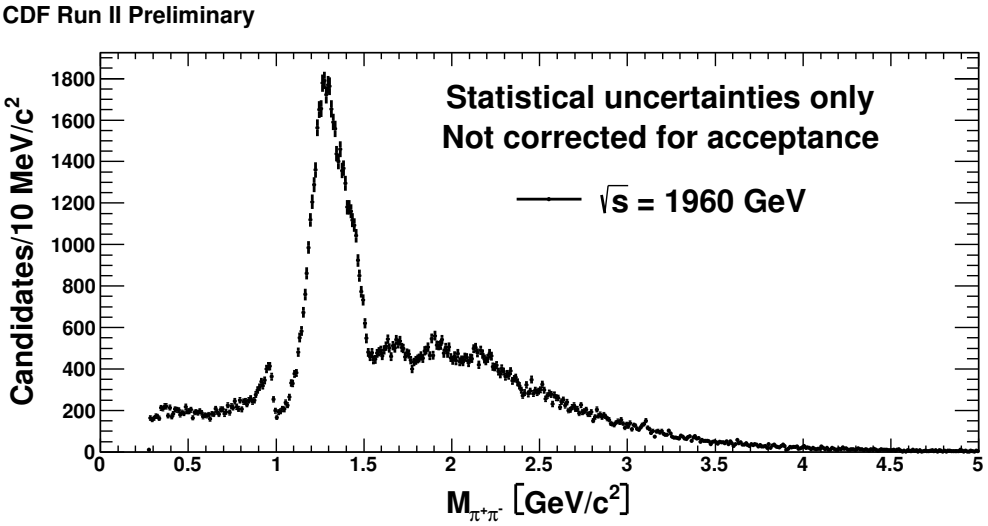

Figure 25: Invariant mass distribution of two particles assuming pion mass - not corrected for acceptance at $\sqrt{s} = 1960$ GeV.

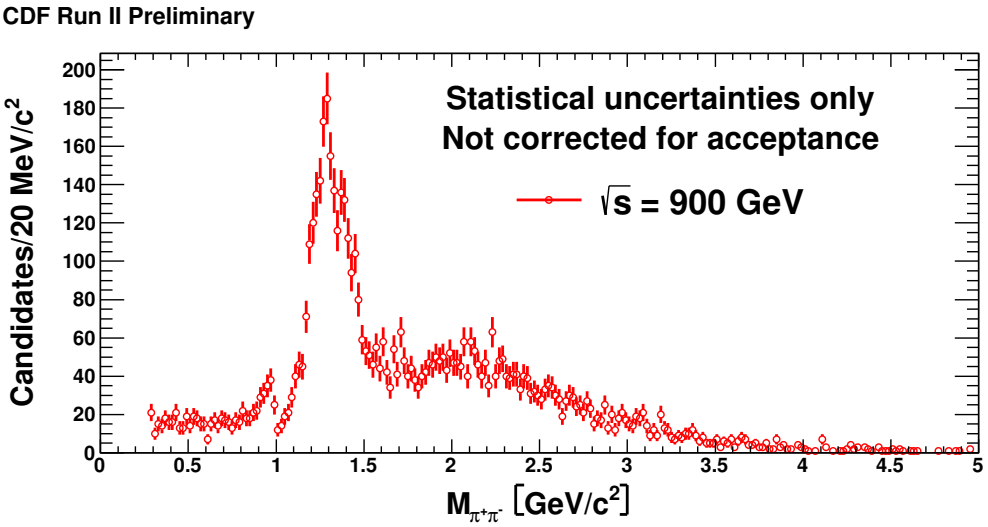

Figure 26: Invariant mass distribution of two particles assuming pion mass - not corrected for acceptance at $\sqrt{s} = 900$ GeV.

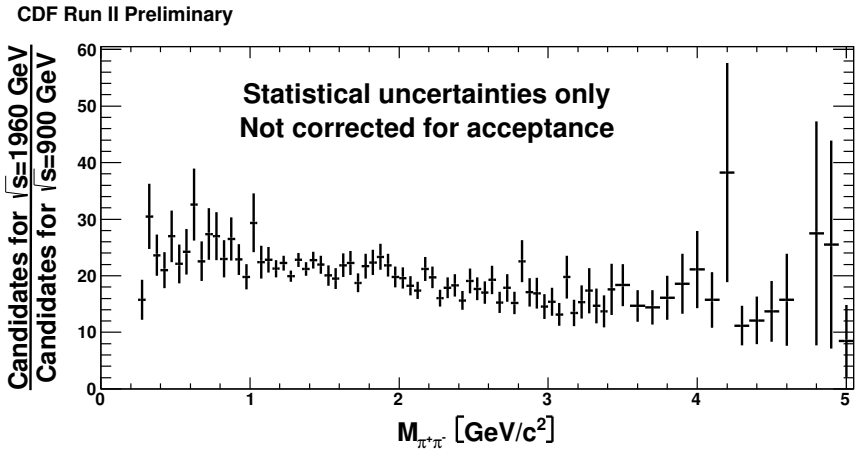

Figure 27: Ratio of numbers of candidate events, not corrected for acceptance or luminosity, as a function of $M(\pi\pi)$.

photoproduction ($\gamma + \mathbb{P}$) but not in D$\mathbb{P}$E (it has C,P = -1,-1). This was not seen in the ISR experiments [12], but they detected both protons with $|t|_{min} = 0.01$ GeV^2 and would not have acceptance for photoproduction (unlike this study, without proton detection). The sharp drop at 1 GeV/c^2, on the high side of the $f_0(980)$, occurs just at the K^+K^- threshold. J.Rosner has argued [11] that when a new channel opens up it causes a "cusp" in the existing scattering amplitudes. The dominant peak between 1.1 GeV and 1.5 GeV is asymmetric and suggests that it includes both the $f_2(1270)$ and the $f_0(1370)$. Rosner has suggested that the "cusp" at 1.5 GeV/c^2 may correspond to the opening of the $\rho\rho$ channel.

7 Acceptance calculation

All cross sections presented are required to be in a certain kinematic region, namely $P_t\,(\text{track}) > 0.4$ GeV/c, $|\eta\,(\text{track})| < 1.3, |y\,(X)| < 1.0$. The P_t and η requirements allow to accept only well-reconstructed tracks. The η and y cuts define the rapidity gap extent.

As the trigger required two towers with $E_T > 0.5$ GeV, a state with $M(X) \lesssim 1$ GeV will not be accepted if it has very small P_t. So the trigger acceptance is a strong function of both $P_t(X)$ and $M(X)$ when these are both small. We also want to avoid low-P_t tracks that are not well reconstructed. For these reasons we require both tracks to have $P_t > 400$ MeV/c.

In order to present cross sections, such as $d\sigma/(dMdP_t)$ in $|y| < 1.0$ we determine the acceptance $A(P_t\,(\pi^+)\,, P_t\,(\pi^-)\,, \eta\,(\pi^+)\,, \eta\,(\pi^-)\,, M_{\pi^+\pi^-}, P_t\,(X)\,, y\,(X))$ using generated samples of MC events. The acceptance as a function of $P_t\,(\pi^+)$,$P_t\,(\pi^-)$,$\eta\,(\pi^+)$ and $\eta\,(\pi^-)$ is calculated using single pion simulation. After reconstruction using CDFSIM the event is checked if the track was reconstructed, and then, if it passed all track quality

Name	M(MeV/c^2)	Γ(MeV)	I^GJ^{PC}	$\pi\pi$	$K\bar{K}$	Other modes
$f_0(600)/\sigma$	400-1200	600-1000	0^+0^{++}	$\sim$100	-	-
$f_0(980)$	980$\pm$10	40-100	0^+0^{++}	dominant	seen	-
$f_2(1270)$	1275.1$\pm$1.2	185$\pm$3	0^+2^{++}	$84.8^{+2.4}_{-1.2}$	4.6 ± 0.4	$2\pi^+2\pi^-$ 2.8%
$f_0(1370)$	1200-1500	150-250	0^+0^{++}	seen	seen	$\rho\rho$ dominant
$f_0(1500)$	1505$\pm$6	109$\pm$7	0^+0^{++}	34.9$\pm$2.3	8.6$\pm$1.0	4π 49.5$\pm$3.3
$f_2'(1525)$	1525$\pm$5	76$\pm$10	0^+2^{++}	0.8$\pm$0.2	88.7$\pm$2.2	$\eta\eta$ 10.4$\pm$2.2
$f_0(1710)$	1720$\pm$6	135$\pm$8	0^+0^{++}	seen	seen	$\eta\eta$ seen
$f_2(1950)$	1944$\pm$12	472$\pm$18	0^+2^{++}	seen	seen	$\eta\eta$ seen
$f_2(2010)$	2011$\pm\sim$ 70	202$\pm\sim$ 70	0^+2^{++}	-	seen	$\phi\phi$ seen
$f_2(2300)$	2297$\pm$28	149$\pm$41	0^+2^{++}	-	seen	$\phi\phi$ seen
$f_2(2340)$	2339$\pm$55	319^{+81}_{-69}	0^+2^{++}	-	-	$\phi\phi$ seen
$f_6(2510)$	2465$\pm$50	255$\pm$ 40	0^+6^{++}	6.0$\pm$1.0	-	

Table 5: Light quark meson states allowed in DIPE. Branching fractions are in %. (PDG 2010)

cuts. The single track acceptance was fitted with the smooth empirical estimate:

$$a\left(\frac{1}{1+exp(b_1P_t+b_2)}+b_3\right)\left(\frac{1}{(1+exp(c_1\eta+c_2))(1+exp(-c_1\eta+c_2))}+c_3\right), \quad (1)$$

where a,b_i and c_i are free parameters. The result is presented in Fig. 28.

The acceptance is dependent not only on single track properties, but on correlations between two tracks. To estimate this contribution, a parent state X is generated, flat in rapidity with $-1.0 < y < +1.0$, in mass and P_t bins from $2m(\pi)$ to 5.0 GeV/c^2, and 0 to 2.5 GeV/c respectively. X is made to decay isotropically (S-wave, J=0) and the quality requirements on each reconstructed track are made. Using that sample, the cuts on 3D opening angle, difference in z between tracks and spatial separation are applied. The number of events that passes such cuts divided by sample size gives the acceptance as a function of $M\,(X)$ and $P_t\,(X)$. The results are presented in the Fig. 29.

The trigger efficiency was determined by a data-driven procedure using well measured isolated tracks from minimum-bias data from same periods. We calculated the probability of track to fire 0, 1, 2 or more trigger towers with $\geqq$4 bits (0.5 GeV) in the 3x3 tower region around the extrapolated tower. The total trigger efficiency is composed of those three probabilities and computed as a function of track P_t and η values. The probabilities as a function of track P_t and η is shown in the Fig. 30.

Finally, in order not to have fake structures from statistical fluctuations in the (finite!) Monte Carlo, we used a bilinear interpolation to compute the acceptance at every point.

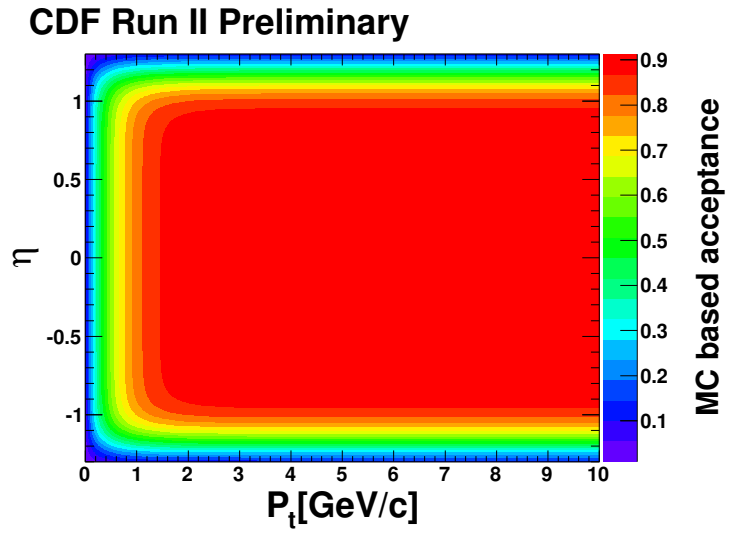

Figure 28: Probability of a track to be reconstructed and to pass quality cuts.

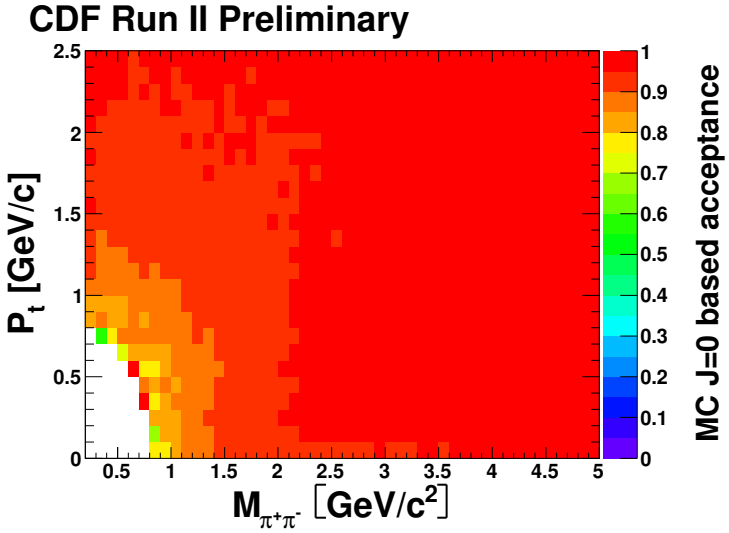

Figure 29: Two track acceptance as a function of invariant mass and P_t after requiring both tracks to be well reconstructed.

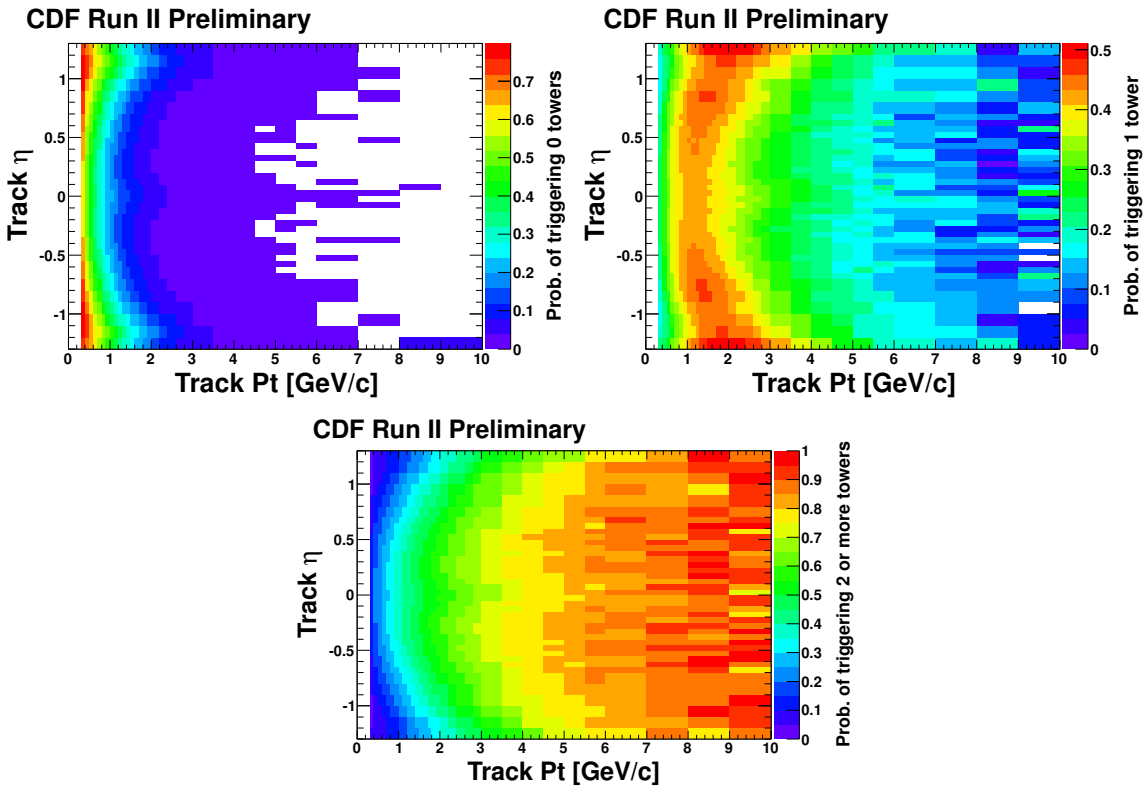

Figure 30: The probability of triggering zero, one and two or more trigger towers as a function of track P_t and η.

8 Systematic uncertainties

To estimate the systematic errors we use the method of loose/tight cuts. We vary a cut by a variation of $\pm 1\sigma$ in the case of Gaussian-like distributions (e.g. P_t), or 0.5*FWHM in case of Lorentz-like distributions (e.g. d_0) or by a reasonable value in case of different cuts (e.g. forward cuts). The resulting shifts in the M, P_t plane are used as systematic uncertainties. Most of the errors are mass-independent The dominant sources of systematic errors are:

- Exclusivity cuts in central region $\approx 15\%$
- Luminosity uncertainty $= 6\%$

The errors are assumed to be uncorrelated. Tables 6 and 7 list the main systematic uncertainties in the cross sections.

Cut	syst. uncertainty in % for $M_{\pi^+\pi^-} < 1.5$ GeV/c^2	syst. uncertainty in % for $M_{\pi^+\pi^-} > 1.5$ GeV/c^2
BSC gap cut	2	2
CLC gap cut	0.1	0.1
Fwd Plug gap cut	4	2
$\eta(\pi)$	0.2	0.2
y(X)	0.1	0.1
3D opening angle	0.1	0.1
d_0	1	1
$P_t(\pi)$	8	2
exclusivity cut	12	9
Δz_0	2	2
COT hits	4	4
χ^2/DoF of track fit	3	3
trigger efficiency	0.4	0.6
stat. error of acceptance	2	4
luminosity	6	6

Table 6: Systematic uncertainties in cross sections distribution for $\sqrt{s} = 1960$ GeV data for low and high invariant mass regions.

In all plots presented in this note, systematic uncertainties are presented as yellow boxes. They were calculated for each distribution bin-by-bin, taking into consideration asymmetries of the uncertainties. Systematic errors in the mean P_t spectrum presented in Section 9.3 are equal to about 1%. They are mostly independent of mass. Systematic uncertainties in the Legendre coefficients spectra, presented in Section 12, are also small and mass-independent. Both of them were calculated using the same method as for the

Cut	systematic uncertainty in % for $M_{\pi^+\pi^-} < 1.5$ GeV/c^2	systematic uncertainty in % for $M_{\pi^+\pi^-} > 1.5$ GeV/c^2
BSC gap cut	2	2
CLC gap cut	0.1	0.1
Fwd Plud gap cut	4	2
$\eta(\pi)$	0.2	0.2
y(X)	0.1	0.1
3D opening angle	0.1	0.1
d_0	1	1
$P_t(\pi)$	12	2
exclusivity cut	15	10
Δz_0	3	3
COT hits	4	4
χ^2/DoF of track fit	4	4
trigger efficiency	0.4	0.6
stat. Error of acceptance	2	4
luminosity	6	6

Table 7: Systematic uncertainties in cross sections distribution for $\sqrt{s} = 900$ GeV data for low and high invariant mass region.

cross sections. All the applied cuts were varied and their influence on the final spectra was checked.

9 $\pi^+\pi^-$ cross sections

For each M, P_t (see Fig. 31) bin we divide the data by the acceptance to get the corrected mass distribution, and use the effective luminosity to get the cross section $d\sigma/dM$. The invariant mass plot integrated over the full P_t range for 1960 GeV is shown in Fig. 32. The comparison of two energies (1960 GeV and 900 GeV) is shown in Fig. 33. Fig. 35 and 34 present ratios of invariant mass distributions for two different $\sqrt{s}$. The invariant mass plot for oppositely charged particles and pairs of particles with the same sign (estimation of non-exclusive background) is presented in Fig. 36. Additionally, to skip the region close to the $P_t(X)$ vs $M(\pi\pi)$ area where two track acceptance equals zero (because of kinematic cut $P_t(\pi)$¿0.4 GeV/c) we are presenting invariant mass distributions for $P_t(X) > 1$ GeV/c and whole mass range, and $P_t(X) < 1$ GeV/c with mass higher then 1 GeV/c^2 for both $\sqrt{s}$ (see Fig. 37 and 37)

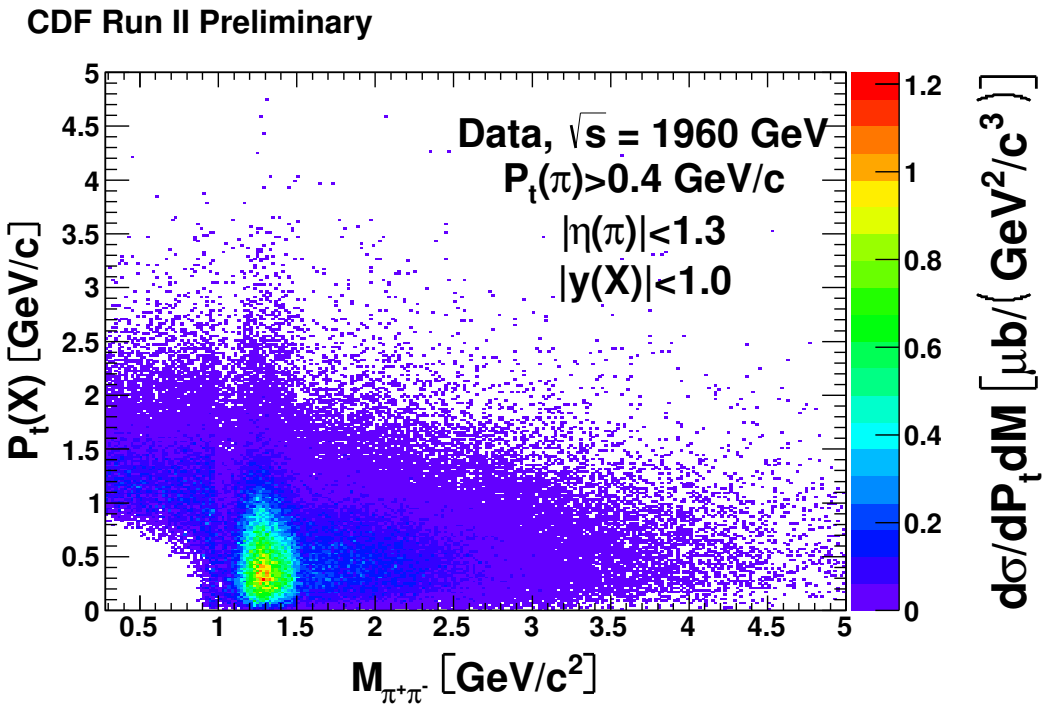

Figure 31: Distribution of events in mass versus P_t for the $\pi^+\pi^-$ central state after acceptance corrections.

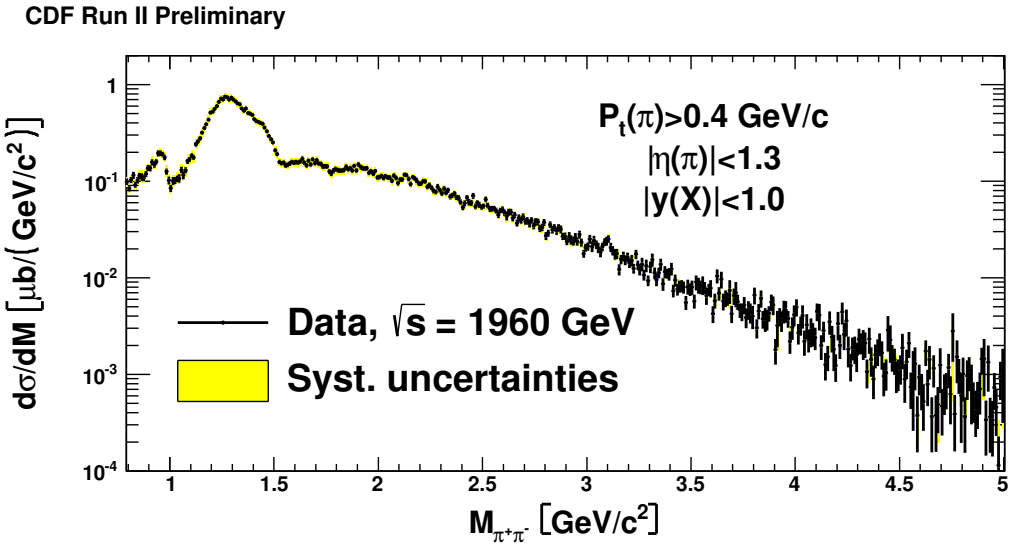

Figure 32: Invariant mass distribution of two particles assuming pion masses - corrected for acceptance, on a logarithmic scale, $\sqrt{s} = 1960$ GeV.

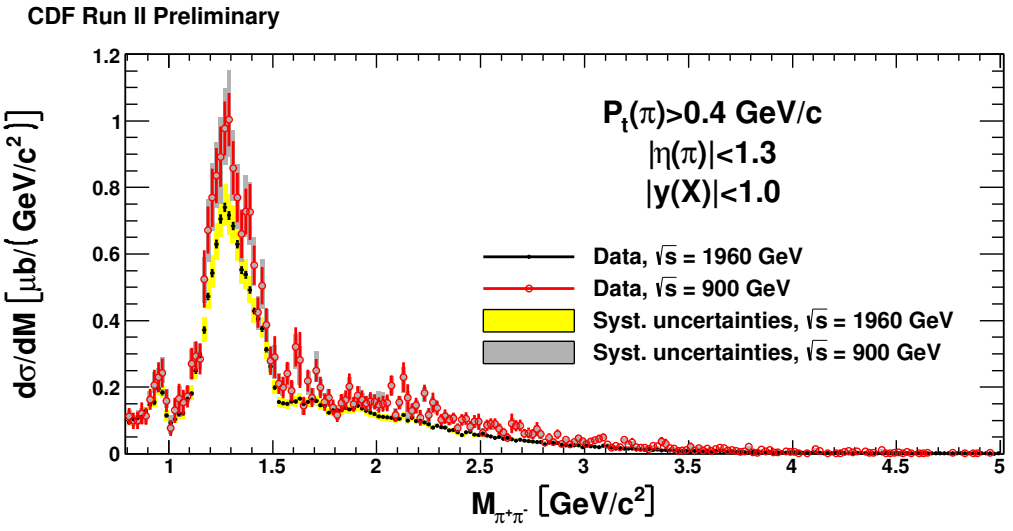

Figure 33: Comparison of invariant mass distribution of two particles assuming pion masses - corrected for acceptance, for two $\sqrt{s}$ energies, 1960 GeV - black and 900 GeV - red.

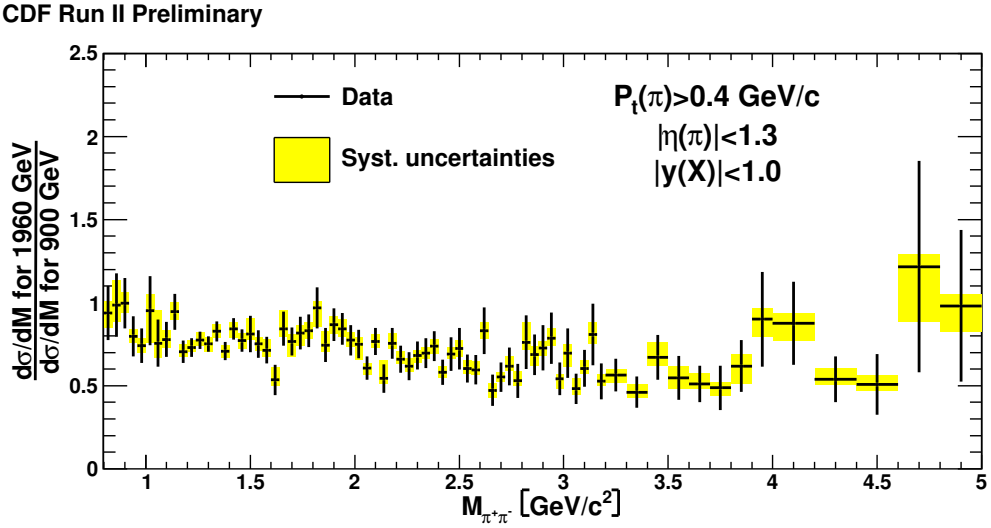

Figure 34: Ratio of cross sections measured at 1960 GeV and 900 GeV.

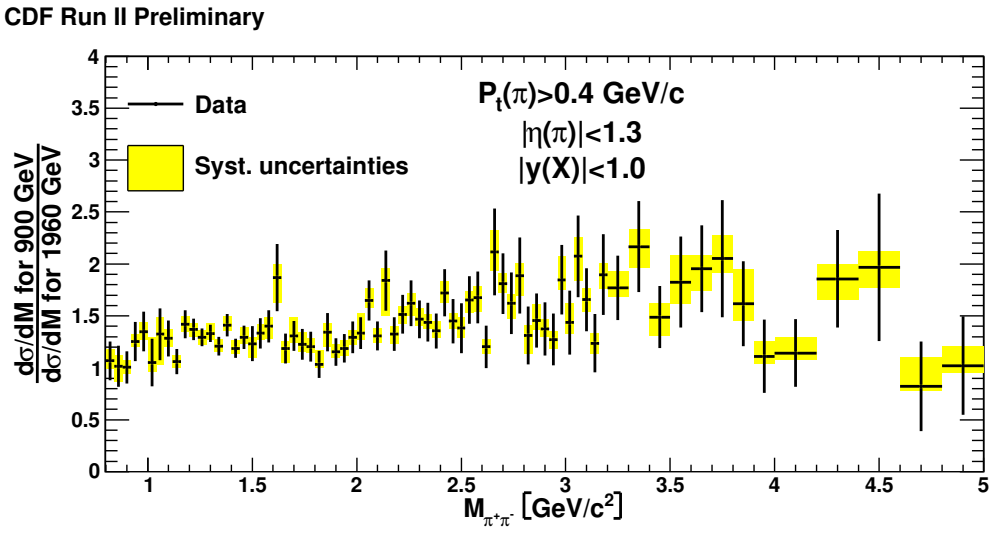

Figure 35: Inverse ratio of cross sections measured at 1960 GeV and 900 GeV.

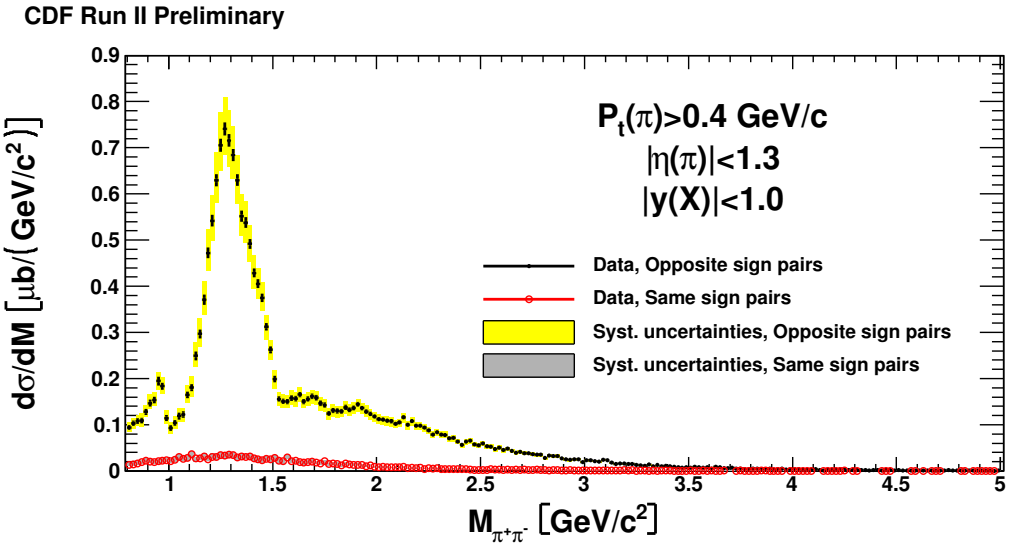

Figure 36: Invariant mass distribution of two particles assuming pion masses - corrected for acceptance, for $\sqrt{s} = 1960$ GeV for opositely charged particles - black and pairs of particles with the same sign - red.

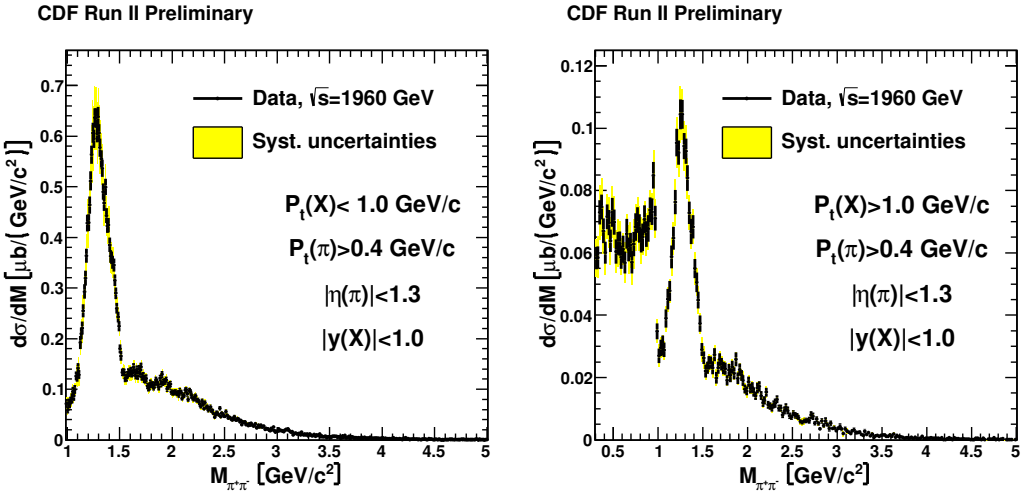

Figure 37: Invariant mass distribution of two particles assuming pion masses for $P_t(X) < 1$ GeV/c (left) and $P_t(X) > 1$ GeV/c (right)for $\sqrt{s} = 1960$ GeV.

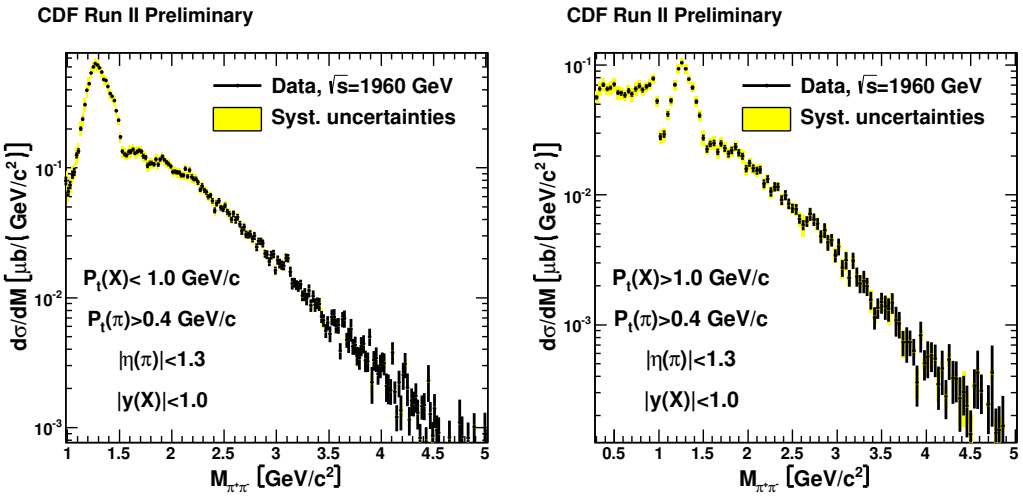

Figure 38: Invariant mass distribution of two particles assuming pion masses for $P_t(X) < 1$ GeV/c (left) and $P_t(X) > 1$ GeV/c (right)for $\sqrt{s} = 1960$ GeV in logarithmic scale.

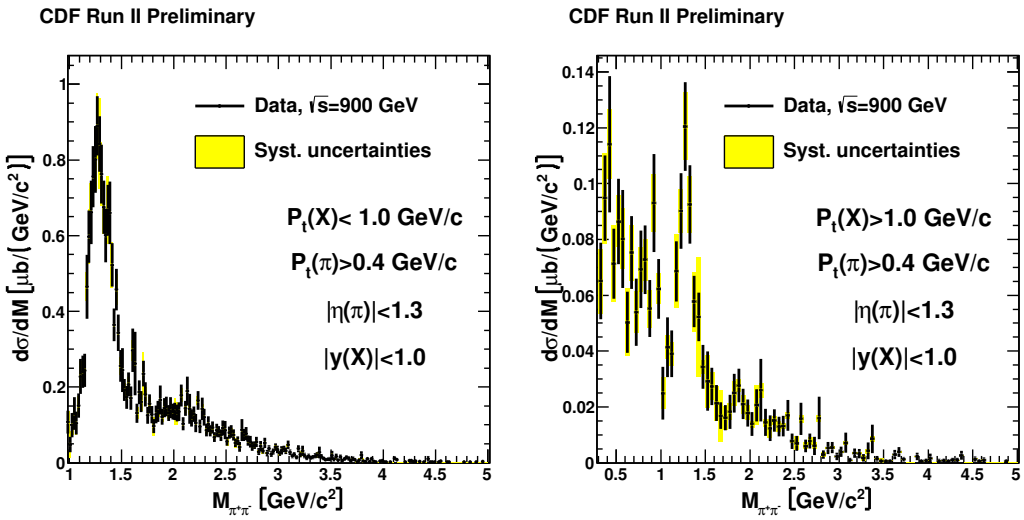

Figure 39: Invariant mass distribution of two particles assuming pion masses for $P_t(X) < 1$ GeV/c (left) and $P_t(X) > 1$ GeV/c (right)for $\sqrt{s} = 900$ GeV.

9.1 Region 0.8-2.0 GeV/c^2

This region consists of the most clearly visible resonances and a continuum $\pi^+\pi^-$ distribution. One can not simply add resonance signals and "background", as they are both results of interference and scattering between the final state pions. We can clearly see the $f_0(980)$ state, a sharp drop at the opening of K^+K^- threshold, then the large peak coming from (probably) the $f_2(1270)$ state, although our partial wave analysis (Section 12) does not support this attribution. This peak shows structure that is not well approximated by single resonance (Breit-Wigner or Gaussian). Above this large peak, at 1.5 - 1.6 GeV/c^2, we see a clear and localized change of slope. All these features are clearly visible in Fig. 40.

9.2 Region $1.6 - 5.0 GeV/c^2$

The region above the most prominent resonances shows a bump structure, not very consistent with simple curve. Some broad f_0/f_2 states might be present there, interfering with a continuum background. Our statistics are not high enough to resolve any such states, but are enough to show the discrepancies from smooth fits. We tried to fit a 4th order polynomial, see Fig. 41, fit to this region, which shows also the residuals. Statistically (black bars) the structures are significant, and the systematic uncertainties (yellow band) are not bin-dependent. The high point at about 3.1 GeV/c^2 is the J/ψ (Section 11).

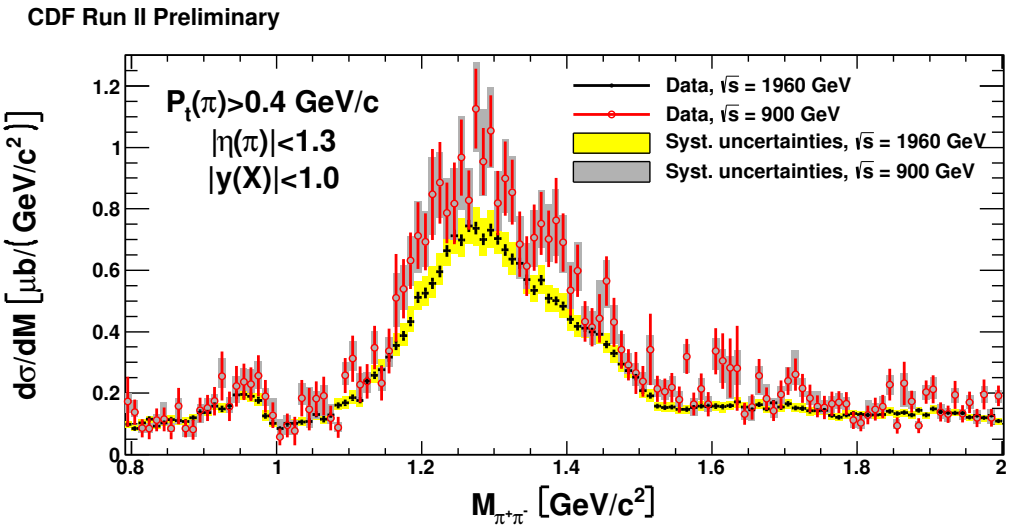

Figure 40: Comparison of invariant mass distribution of 2 particles assuming pion masses - corrected for acceptance, for two $\sqrt{s}$ energies, 1960 GeV - black and 900GeV - red.

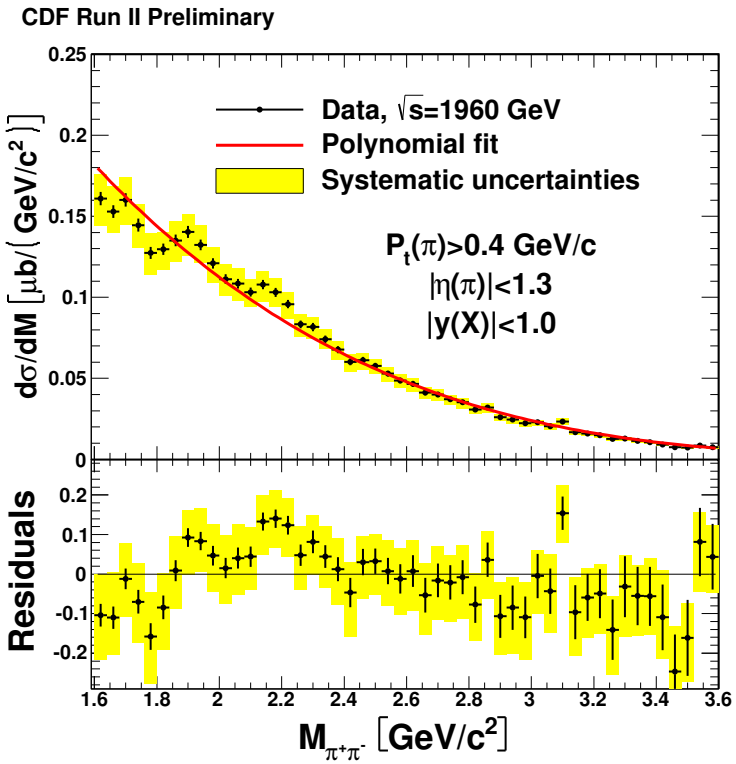

Figure 41: Invariant mass distribution of 2 particles assuming pion masses - corrected for acceptance with 4th order polynomial fit together with residuals of the fit, $\sqrt{s}$ = 1960 GeV.

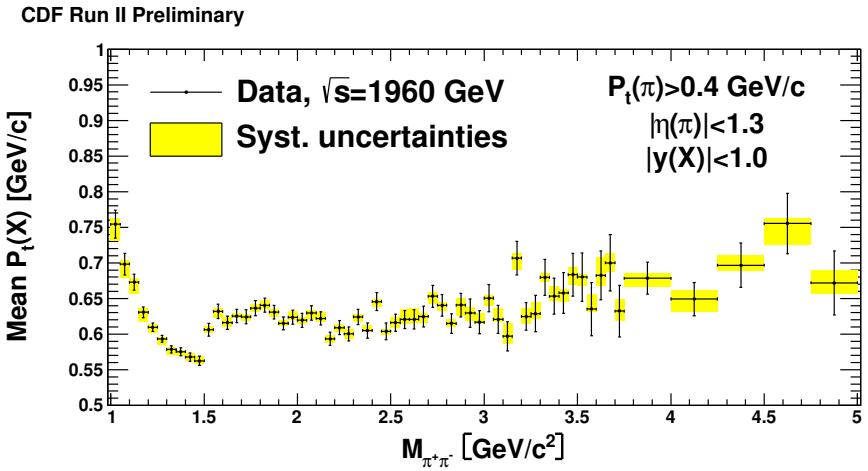

Figure 42: Mean value of the P_t distribution of the central state decaying to two central pions as a function of invariant mass, $\sqrt{s} = 1960$ GeV.

9.3 Mean P_t

Another interesting kinematic variable is the P_t of central state. In Figs. 42 and 43 show the dependence of $\langle P_t \rangle$, corrected for acceptance, on the invariant mass. This distribution shows interesting structure not significantly dependent of the $\sqrt{s}$ energy. It has been already shown that the acceptance has a cut-off at low P_t for $M(\pi\pi) < 0.8$ GeV/c^2, so we only show this for $M(\pi\pi)$ >1 GeV/c^2 where the acceptance distortion is not too strong. The main feature of this plot is the rather localized increase in $\langle P_t \rangle$ at 1.5 GeV/c^2, coinciding with the change in slope of the mass spectrum, and not due to any rapid change of the acceptance. There may also be some features above 2 GeV/c^2. A few of the distributions of P_t (for some mass ranges) are shown in Fig. 44.

10 Exclusive χ_{c0} production in $\chi_{c0} \to \pi^+\pi^-$ and K^+K^-.

We previously observed [6] exclusive DIPE production of $\chi_c(c\bar{c}) \to J/\psi + \gamma \to \mu^+\mu^-\gamma$ with a cross section $d\sigma/dy|_{y=0} = 76 \pm 10(\text{stat}) \pm 10(\text{syst})$ nb (7.6×10^{-32} cm^2), *assuming* all the events were $\chi_{c0}(3415)$. This corresponded to 65 candidate events. The process is especially important because the χ_{c0} has the same quantum numbers as the Higgs boson (apart from its strong interactions) and is produced the same way but with a c-loop replacing the t-loop, so it is a good control of the theoretical calculations. Unfortunately in the exclusive $\chi_c \to J/\psi + \gamma$ channel the photon is soft and the mass resolution of $J/\psi + \gamma$, together with the poor energy resolution of the EM calorimeter, did not allow a separation of the three χ_c^0 states. The J=1 and J=2 states should theoretically be suppressed in production (in DIPE) but they have larger branching fractions to this mode, see Table 9, which also shows the decays to only charged hadrons that have branching fractions $\gtrsim 0.1\%$ for the χ_{c0}.

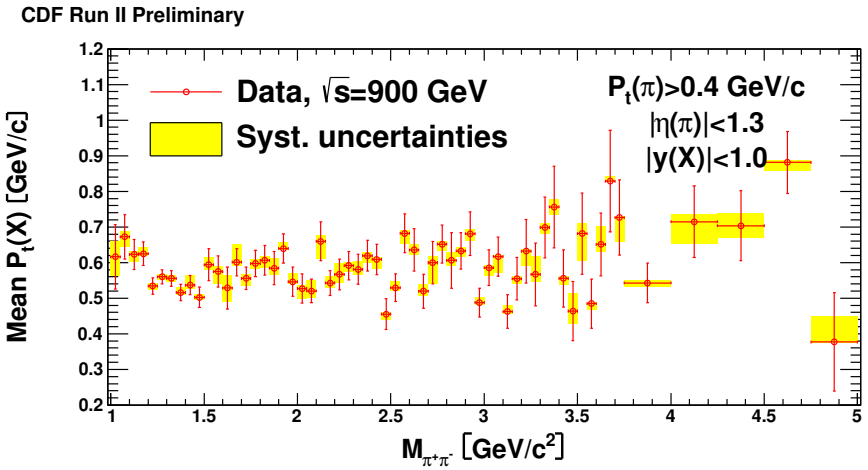

Figure 43: Mean value of the P_t distribution of central state decaying to two central pions as a function of invariant mass, $\sqrt{s}$ =900 GeV

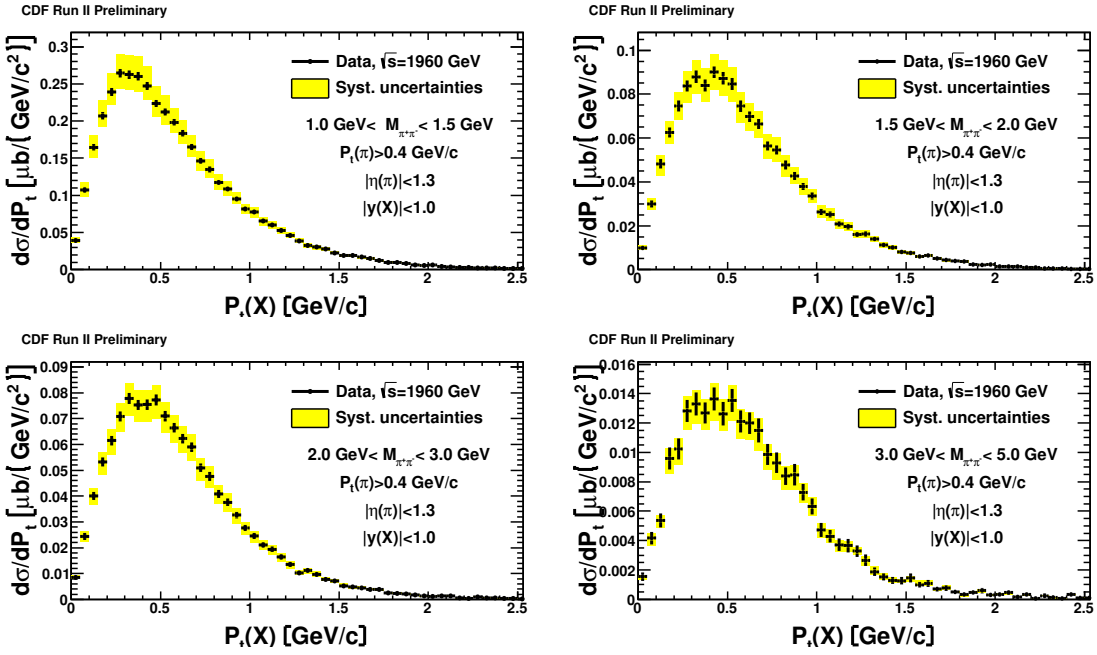

Figure 44: P_t distribution of central state decaying to two central pions in few mass windows, $\sqrt{s}$ =1960 GeV.

As we could not resolve the three χ_c states we actually measured $\sum_{i=0,2} B_{ci}.\sigma_{ci}$ where the branching fractions to $J/\psi+\gamma$ from the PDG [16] are given in Table 9. Even though the $\chi_{c1}(3511)$ and $\chi_{c2}(3556)$ are theoretically very suppressed they may contribute a lot to the $J/\psi+\gamma$ signal. Observation in the $\pi^+\pi^-$ and K^+K^- channels can resolve the states, not only because the mass resolution $\sigma(m) \sim 25$ MeV is less than their separation but also because the decay fractions are higher (than the combination $\chi_c \to J/\psi+\gamma \to \mu^+\mu^-+\gamma$). In the two cases, "all χ_{c0}" or "a mixture of all three" (B = branching fraction):

$$B_{c0}\sigma_{c0}(\mathrm{if-alone}) \equiv [B_{c0}\sigma_{c0} + B_{c1}\sigma_{c1} + B_{c2}\sigma_{c2}](\mathrm{if-all-three})$$

and dividing through by B_{c0}:

$$\sigma_{c0}(\mathrm{if-alone}) \equiv \sigma_{c0} + (B_{c1}/B_{c0} = 26.8) \times \sigma_{c1} + (B_{c2}/B_{c0} = 17.1) \times \sigma_{c2}$$

Let us take as an example the predictions of Teryaev, Pasechnik and Szczurek [21] for the relative cross sections $d\sigma/dy|_{y=0}$ of the three states. There are large uncertainties, depending on parameters, but they expect approximately $\sigma_{c0} : \sigma_{c1} : \sigma_{c2} = 1.0 : 0.006 : 0.09$. In that example we would have:

$$\sigma_{c0}(\mathrm{true}) = \sigma_{c0}(\mathrm{if-alone}) \times 1/(1 + 26.8 \times 0.006 + 17.1 \times 0.09) = 0.37 \times \sigma_{c0}(\mathrm{if-alone})$$

and then σ_{c0}(true) would be $\sim 0.37\times$ 76nb = 28 nb.

LHCb have reported [22] (unpublished) an "exclusive" $M(J/\psi+\gamma)$ distribution fit to the sum of the three (unresolved) states at $\sqrt{s} = 7$ TeV. As in CDF they do not detect the protons, so it also includes dissociation, and the χ_c are forward ($+2 < y < +4$) so the data are not directly comparable. However their fit shows that only about 17% of the $J/\psi+\gamma$ events are from the χ_{c0}, while after correcting for the branching fractions the states are produced in the ratios $1 : 0.06 : 0.20$ (for uncertainties see the numbers in Ref. [22]).

The new $\pi^+\pi^-$ and K^+K^- data presented here can provide a measurement (in practice an upper limit) of $d\sigma/dy|_{y=0}$. The data in Fig. 32 do not show a significant $\chi_{c0}(3415)$ signal. In Fig. 45 we show the number of events between 2.5 and 5.0 GeV/c^2 together with a fit excluding the regions of the J/ψ and $\chi_{c0} \to \pi^+\pi^-, K^+K^-$ (with the K given the pion mass). The fit is an exponential with slope -1.876 GeV^{-1}. Table 8 presents results. They rule out the supposition that all the $J/\psi+\gamma$ events in Ref.[6] were from χ_{c0}[1], and would be consistent with the 17% fraction seen by LHCb (although they are at a different $\sqrt{s}$ and in a different y-region, and also not published).

11 Evidence for $J/\psi \to e^+e^-$

The mass distribution has a small excess in the vicinity of the $J/\psi(3097)$. Photoproduction of J/ψ with decays to $\mu^+\mu^-$ was previously observed in CDF [6], with $d\sigma/dy(y=0)$

[1] In that paper we allowed for this by also quoting $\sum B_{ci}\sigma_{ci}$.

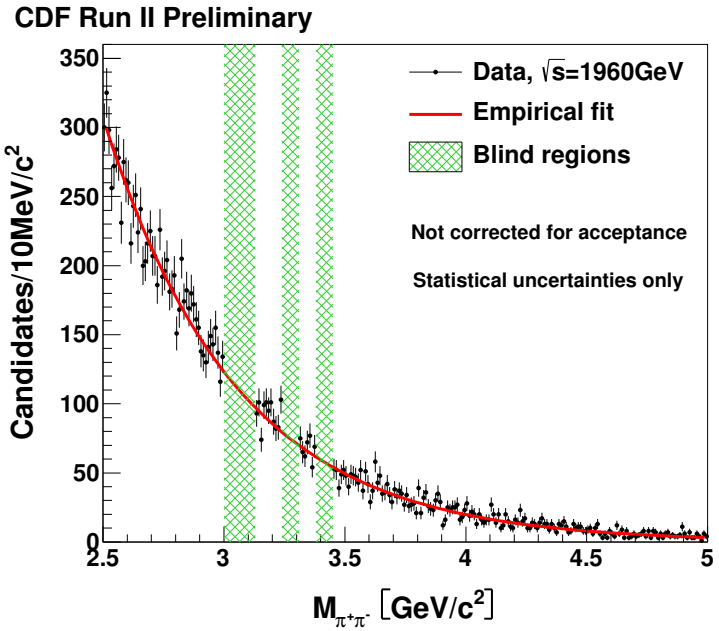

Figure 45: Invariant mass distribution of two particles, assumed to have $m(\pi)$, in the charmonium region at $\sqrt{s} = 1960GeV$. The regions of the J/psi and χ_{c0} (in both $\pi^+\pi^-$ and K^+K^- modes) are excluded from the fit.

Table 8: Upper limits on χ_{c0} cross sections.

State:	$\chi_{c0} \to \pi^+\pi^-$	$\chi_{c0} \to K^+K^-$
Background (est.)	404.4	522.1
Events in window	424	515
90% CL upperlimit (events)	49.3	34.6
Acceptance	21.4%	21.3%
$d\sigma/dy\|_{y=0}$, 90% CL UL	35.5±2.1 (syst.) nb	23.4±1.4 (syst.) nb

Table 9: Branching fractions (BF in %) of χ_c states, for decays to all charged particles with BF $> 0.1\%$.

State $I^G J^{PC}$	$\chi_{c0}(3415)$ 0^+0^{++}	$\chi_{c1}(3511)$ 0^+1^{++}	$\chi_{c2}(3556)$ 0^+2^{++}
Mass(MeV): Width (MeV): BF(Channel)	3414.76±0.35 10.4±0.7	3510.66±0.07 0.89±0.05	3556.20±0.09 2.06±0.12
$J/\psi + \gamma$ Above with $J/\psi \to \mu^+\mu^-$	1.16±0.08 0.077	35.6±1.9 0.021	20.2±1.0 0.012
$\pi^+\pi^-\pi^+\pi^-$	2.27±0.19	0.76±0.26	1.11±0.11
$\pi^+\pi^-K^+K^-$	1.80±0.15	0.45±0.10	0.92±0.11
$3(\pi^+\pi^-)$	1.20±0.18	0.58±0.14	0.86±0.18
$\pi^+\pi^-$	0.56±0.03	<0.1	0.159±0.009
K^+K^-	0.60±0.03	<0.1	0.11±0.008
$\pi^+\pi^-K^0_sK^0_s$	0.58±0.11	<0.1	0.92±0.11
Above with $K^0_S \to \pi^+\pi^-$	0.27±0.05	<0.1	0.43±0.05
$K^+K^-K^+K^-$	0.28±0.03	0.06±0.01	0.18±0.02
$\pi^+\pi^-p\bar{p}$	0.21±0.07	<0.1	0.13±0.03
Total %	7.2	1.9	4.7

= 3.92±0.62 nb, compared with several theoretical predictions for $p + \bar{p} \to p + J/\psi + \bar{p}$ from 2.8 - 3.4 nb. The measured CDF value had been reduced by $9 \pm 2\%$ to account for unseen fragmentation, with $|\eta| > 7.4$. The present measurements allow fragmentation with products between $|\eta| = 5.9$ and $y(\text{beam}) = 7.64$ and so should be larger. The only non-rare J/ψ decays to just two tracks are to e^+e^- and $\mu^+\mu^-$, each about 5.9%. Most of the $\mu^+\mu^-$ decays should be excluded by our muon stub cut. The e^+e^- events should be in our sample. Those events, with the tracks incorrectly given the pion mass, should appear at about 3.112 MeV, only 12 MeV higher. (Any $\mu^+\mu^-$ events would be at about 3.105 MeV. These are values for a J/ψ at rest, but are approximately true for our kinematics.) To quantify the excess in this data we fitted the mass distribution over the range $2.9 < M(\pi^+\pi^-) < 3.5$ GeV/c^2 to a linear background, excluding 3.06 - 3.14 GeV, plus a Gaussian constrained to have a peak in that range but otherwise with centre, width and size floating. See Fig. 46. The fit gives mean value at 3.097 ± 0.003 GeV/c^2, width $\sigma = 12.7$ MeV/c^2 and significance 4.46σ

We can assume the events are mostly $J/\psi \to e^+e^-$, since most $\mu^+\mu^-$ decays will be excluded by the muon stub veto. Simply as a check that the apparent signal is reasonable in magnitude, we count the excess events in the fitted peak (76), and with an acceptance for $J/\psi \to \ell^+\ell^-$ of 20% (compared with 24.2% for $\chi_{c0} \to \pi^+\pi^-$), using the B.R in Table 9, we find $d\sigma/dy|_{y=0}(J/\psi) = 2.67$ nb. We do not give errors, as we do not think a full error analysis is worthwhile (in contrast our observation [6] in the

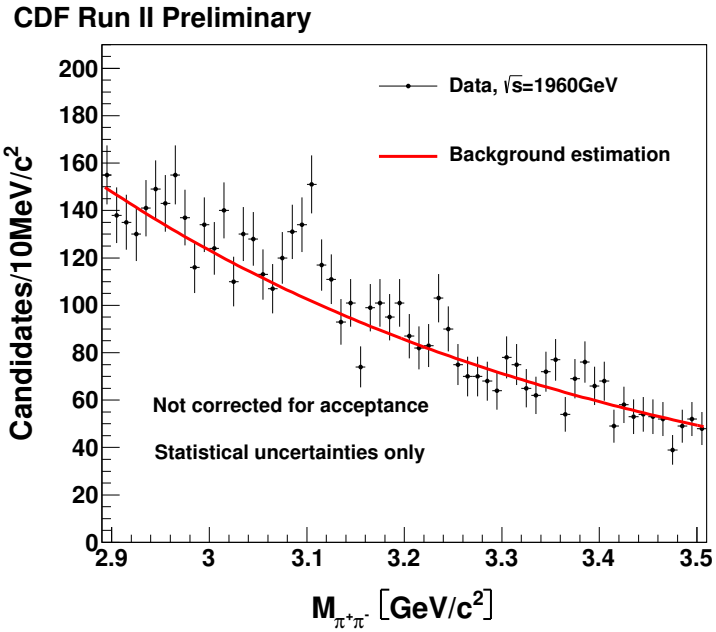

Figure 46: Invariant mass distribution of 2 particles in the J/ψ region. with the same fit as in Fig. 45, which excludes $M(J/\psi) \pm 3\sigma$.

$\mu^+\mu^-$-channel had practically zero background). Our paper [6] gave $d\sigma/dy|_{y=0}(J/\psi)$ $= 3.92 \pm 0.25$ (stat) $\pm$ 0.52(syst) nb. Clearly our new data is consistent with this, and we can conclude that the peak in Fig. 46 is indeed the J/ψ; this verifies that our mass scale is correct to about 12 MeV, and the mass resolution is better than $\sigma = 15$ MeV.

12 Partial Wave Analysis

In the AFS experiment [12] both protons were measured as well as the central $\pi^+\pi^-$. A partial-wave analysis (PWA) was done and showed the data to be dominated by S-wave (J=0) below 1.1 GeV/c^2, apart from a small P-wave at the ρ-mass, not visible in the mass distribution, and assumed to be ρ-photoproduction. A small D-wave signal is present between 1.2 and 1.5 GeV/c^2 and again at higher masses, see Fig. 11b of Ref. [12]. In this data we do not have the forward protons, which can therefore dissociate, and due to the rapidity gap requirement we have a rather limited angular acceptance. However, we can distinguish between different spin behavior by comparing data to MC sample with pre-defined spin content.

As a first step we test the "S-wave only" hypothesis, by comparing $\cos\theta$ distributions (θ - production angle) of data and Monte Carlo. To do this, we use the the Smirnow test with λ-Kolmogorov statistics, taking anything other than pure S-wave as an alternative hypothesis. The test is done in mass bins of 50 MeV/c^2 from 0-2 GeV/c^2, 100 MeV/c^2 from 2-4 GeV/c^2 and 200 MeV/c^2 from 4-5 GeV/c^2. The p-value of the

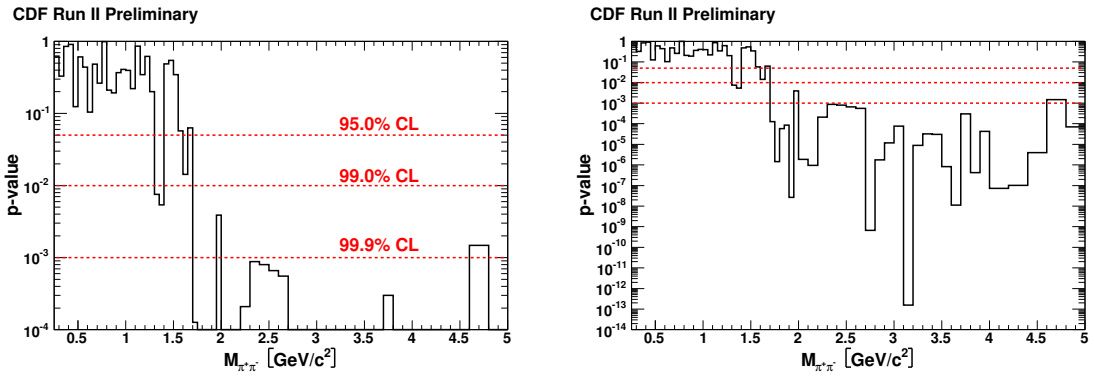

Figure 47: (Left)p-value of Smirnow test on S-wave only hypothesis as a function of mass for $\sqrt{s} = 1960$ GeV data. We exclude the S-wave only hypothesis at 99.9% C.L. above an invariant mass of 1.51 GeV/c^2. (Right) The same plot on an extended scale.

test is shown in Fig. 47. Above 1.5 GeV/c^2 the pure S-wave hypothesis is excluded at 99% C.L. The $\cos\theta$ versus invariant mass distribution is shown in Fig. 48, and on 1-dimensional plots in several mass ranges in Fig. 49. In Fig. 50 the shape of the $\cos\theta$ distribution in the data is compared with distribution from Monte Carlo-generated samples assuming pure S-wave state content.

12.1 Legendre polynomials

To do a more detailed analysis of spin content we decompose the $\cos\theta$ distribution in Legendre polynomials. Following the Jacob and Wick formula [23] for the $a+b \to c+d$ cross section:

$$\begin{aligned}\frac{d\sigma}{d\Omega} &= \frac{1}{(2s_a+1)(2s_b+1)p^2}\sum_{(\lambda),J,J'}\left(J+\frac{1}{2}\right)\left(J'+\frac{1}{2}\right)(-1)^{\lambda-\mu}\cdot \\ &\cdot \langle\lambda_a\lambda_b|\,T_J(E)\,|\lambda_c\lambda_d\rangle^*\langle\lambda_a\lambda_b|\,T_{J'}(E)\,|\lambda_c\lambda_d\rangle\cdot \\ &\cdot \sum_\ell C(JJ'\ell;\lambda,-\lambda)\,C(JJ'\ell;\mu,-\mu)\,P_\ell(\cos\theta)\,,\end{aligned}$$

we estimate the coefficients in front of each Legendre polynomial by calculating the weighted average:

$$a_l = \frac{\sum_i w_i P_l(\cos\theta_i)}{\sum_i w_i}, \tag{2}$$

where the sum is done over all events and w_i are weights obtained from the acceptance. We did the same analysis using MC events generated with S-wave only. In that situation one expects, having full kinematic coverage, all coefficients except the 0^{th} to be zero (i.e. the $\cos\theta$ distribution is flat). Unfortunately, our kinematic cuts on track P_t and η strongly influence the shape of the $\cos\theta$ distribution. Results of this coefficient estimation are presented in Fig. 51.

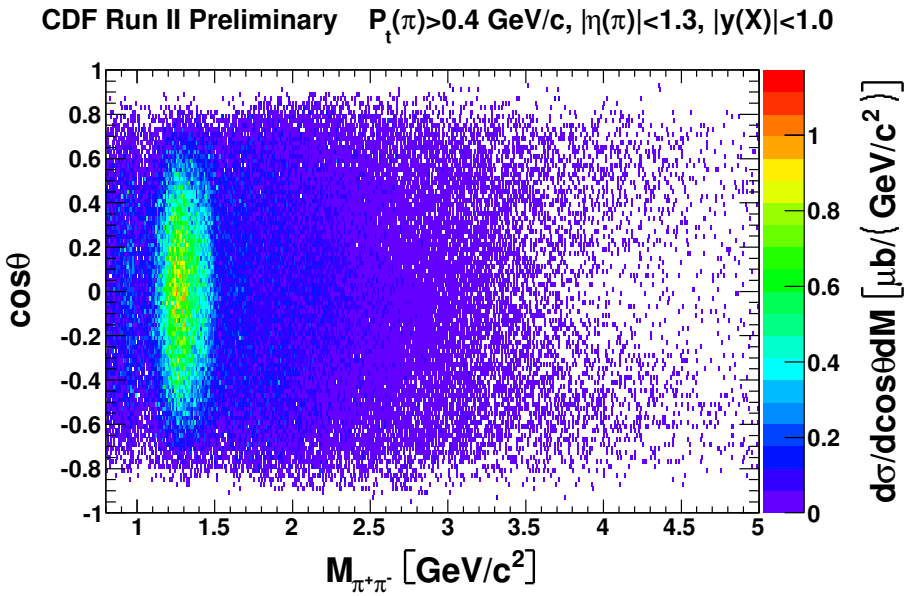

Figure 48: The differential cross section as a function of invariant mass and $\cos\theta$ for $\sqrt{s} = 1960$ GeV.

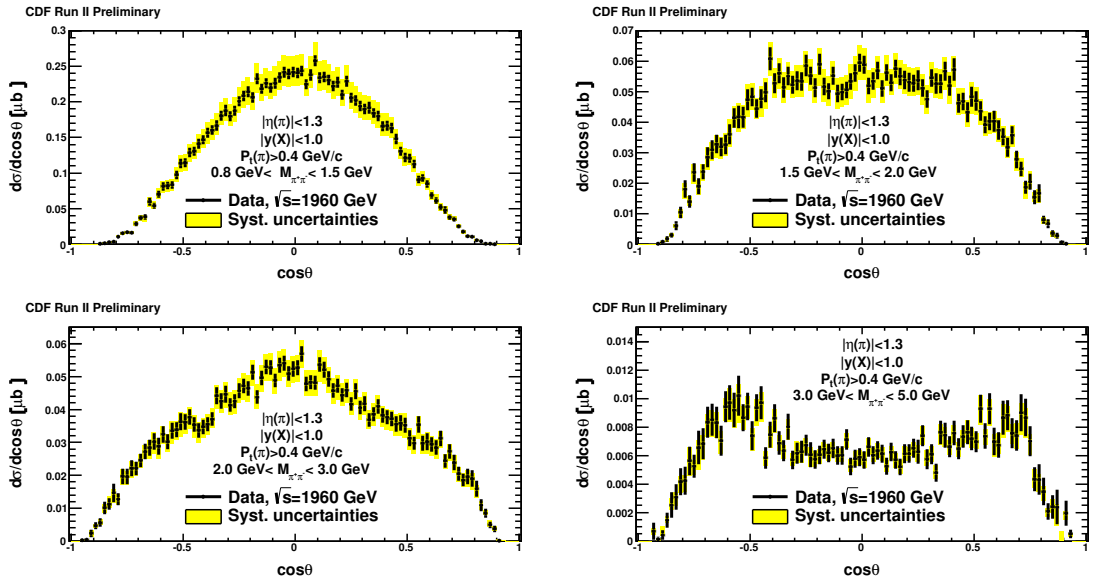

Figure 49: Differential cross section as a function of $\cos\theta$ in several mass bins.

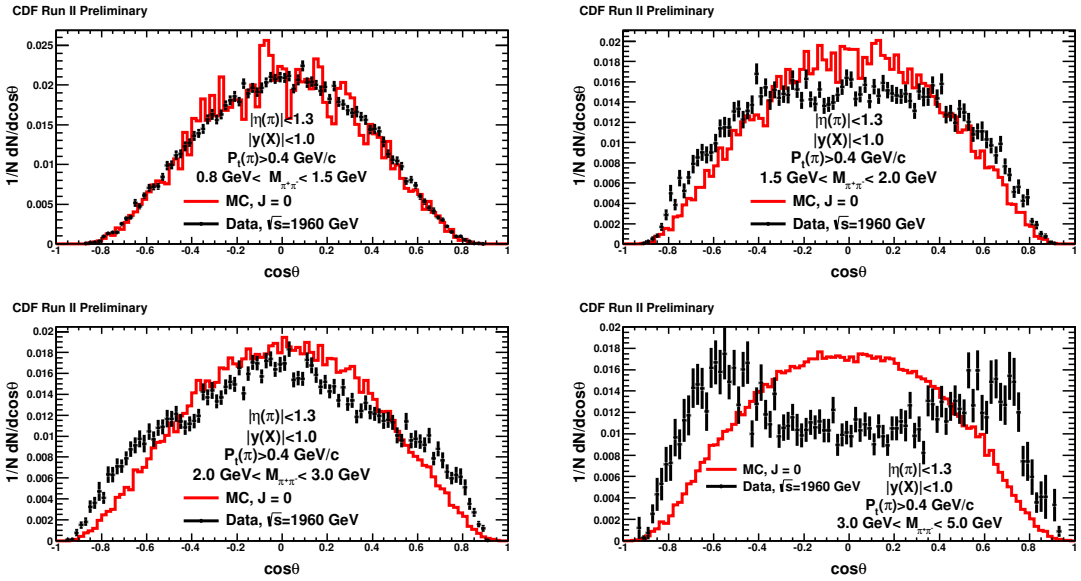

Figure 50: Normalized $\cos\theta$ distribution in several mass bins for our data compared to MC sample with isotropic decay mode (pure S-wave).

We conclude that up to $M(\pi^+\pi^-) = 1.5$ GeV/c^2 the data are consistent with being only (or at least, dominated by) S-wave, while above that higher waves must be introduced. We do not see a local dip in the p-value that could be caused by a dominant $f_2(1270)$ meson.

13 K^+K^- background in $\pi^+\pi^-$ data.

13.1 Charged track identification

Thus far we have been assuming that the two charged hadrons are $\pi^+\pi^-$, without using any hadron identification. There are three main ways of estimating the K^+K^- background in each mass bin. One is to use the ionization of the COT tracks, i.e. dE/dx, which depends on the particle speed and hence its mass (for a given momentum). Fig. 52 shows a plot of dE/dx vs. track momentum, and Fig. 53 shows the distribution of dE/dx for tracks with momentum 400 - 450 MeV/c.

Secondly one can use the flight time from the collision time to the Time of Flight (TOF) counters. For these exclusive h^+h^- events the actual collision time (t_0) is not known within about 1 ns, and the two hadrons will tend to arrive simultaneously at the TOF counters no matter what their identity. However there will be a time difference between the two hadrons at the ToF if the momenta and/or path lengths are different.

To check contribution of K^+K^- events in our data sample the Time of Flight method was used. For each two tracks event, which passed all cuts described in Sec. 6 and 4, exactly 2 ToF matches were required. 37% of our selected events passed this

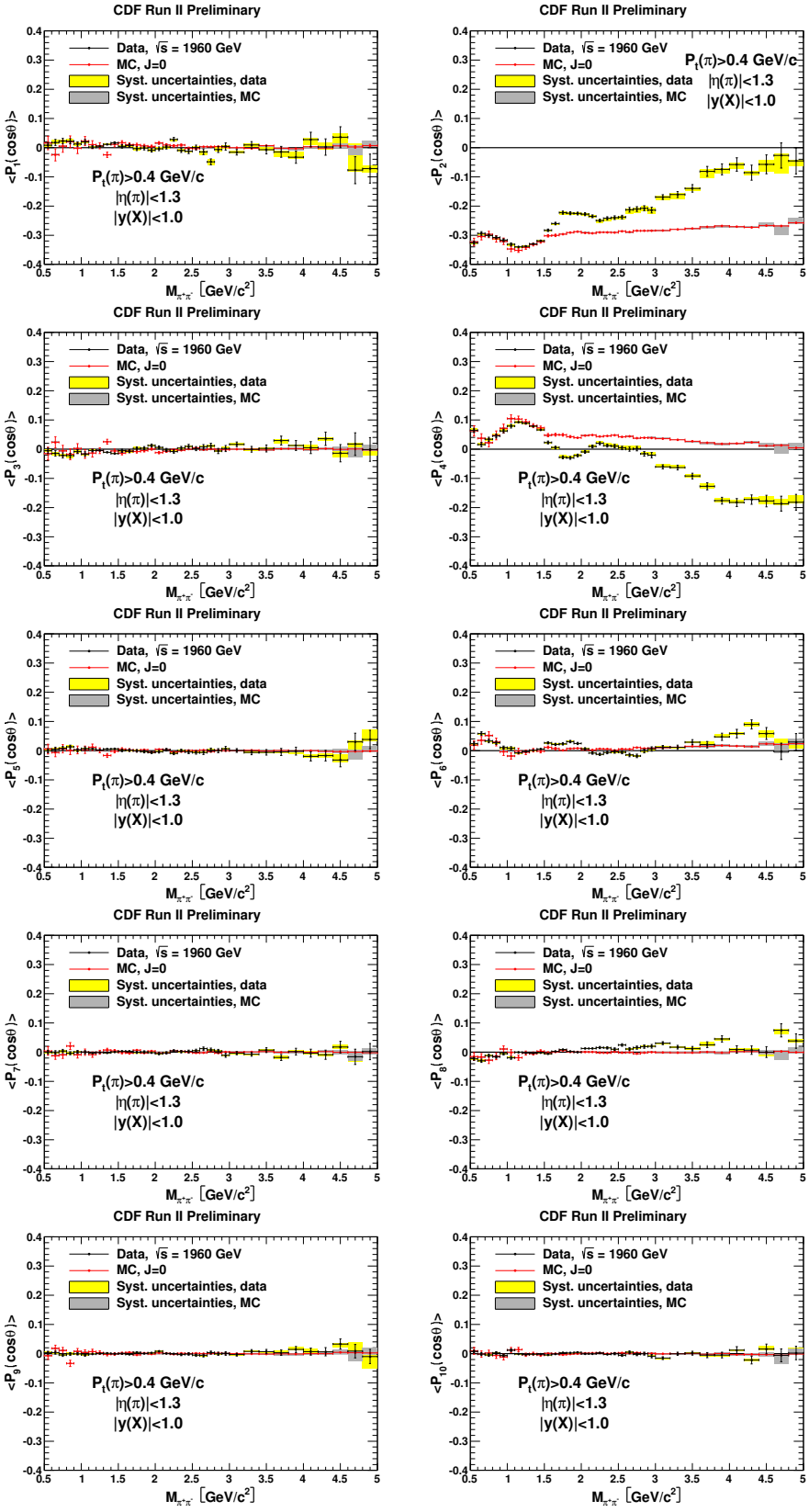

Figure 51: First ten Legendre coefficients as a function of mass for selected sample of two tracks events for $\sqrt{s} = 1960$ GeV data and for MC sample (isotropic decay model) of two tracks events.

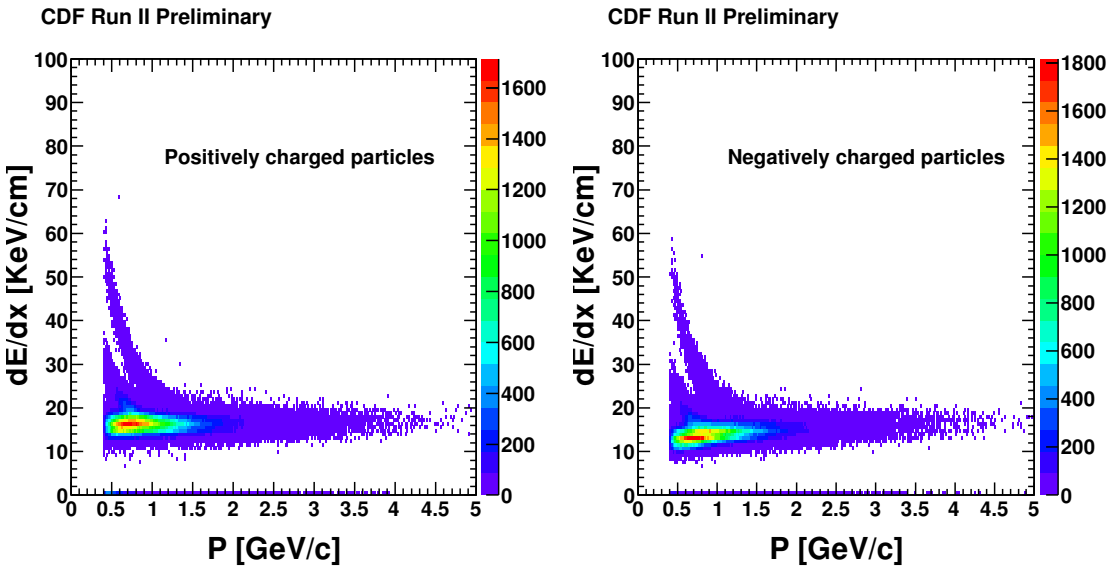

Figure 52: dE/dx versus track momentum for positively and negatively cherged perticles.

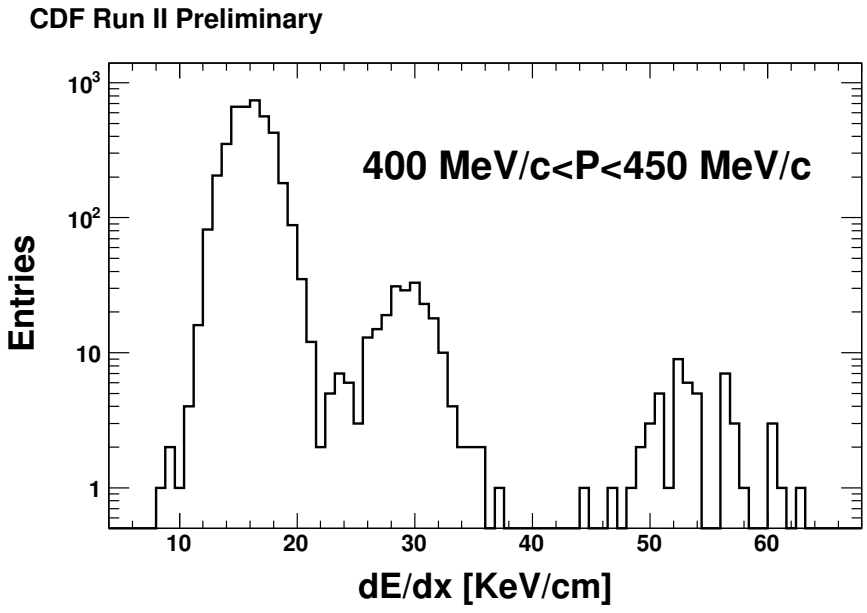

Figure 53: Distribution of dE/dx for tracks with momentum 400-450 MeV/c for positively charged particles.

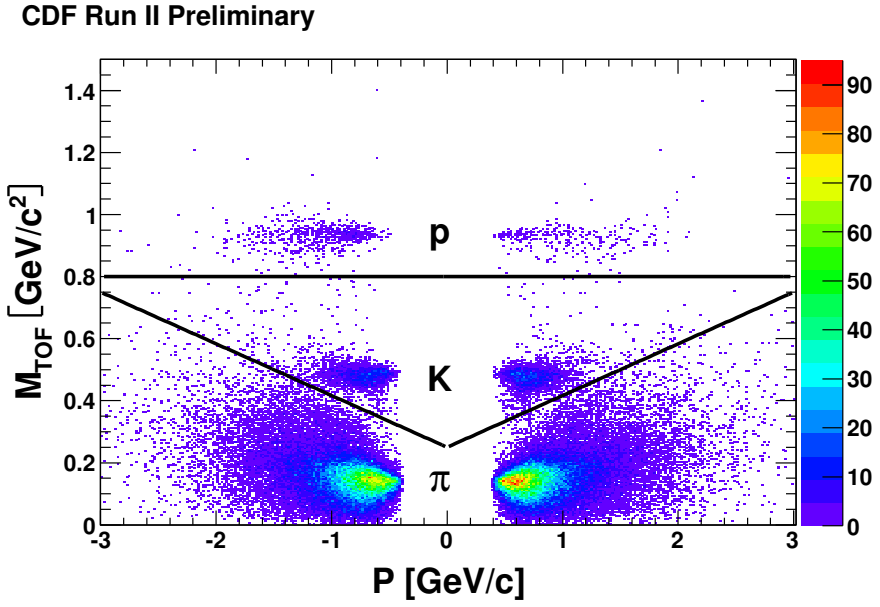

Figure 54: Mass calculated using Time of Flight as a function of particle momentum. Visible bands correspond to pions, kaons and protons respectively. Negative momenta correspond to negatively charged paricles.

requirement ($\epsilon_{TOF} = 37\%$). The fraction is small primarily because the TOF counters are more limited in $|\eta|$ than the tracking. In Fig. 54 mass calculated using TOF (M_{TOF}) versus particle momentum is shown. The negative momenta correspond to paricles with negative charge. Fig. 55 presents the M_{TOF} for whole momentum range for negatively and positively charged particles. To separate $\pi/K/p$ sharp cuts presented as black lines in Fig.54 were used. The momentum-dependent cut is empirical, to avoid the dominant pions feeding into the kaon band at high momentum, where the mass resolution is poor. It was chosen to follow the valley between pion and kaon clusters. We assume that all particles with M_{TOF} smaller then $(0.25 + p \cdot 0.1667)$ GeV/c^2, where p ia a particle momentum, are pions. Particles with $(0.25+p\cdot 0.1667)$ GeV/c^2 $< M_{TOF} <$ 0.8 GeV/c^2 are kaons, and remaining particles are assumed to be protons. The percentage contents of all types particles pairs are presented in Table 13.1. Fig.56 presents the obtained mass distribution assuming mass od two pions π with contributions coming from KK, πK, and Kp, πp, $p\bar{p}$ pairs.

The K^+K^- and $p\bar{p}$ events will be the subject of a future paper. A somewhat larger background is the ∼10% of events with the tracks identified as $K^+\pi^-$ or $K^-\pi^+$. These could be missing a pair of charged particles, or possibly a K^0_L which does not give a big enough signal in the calorimeters to be removed by the exclusivity cut. We show these backgrounds in Fig. 56, assigning pion masses to both particles. As for the Q = 2 events, we do not subtract them from the spectra.

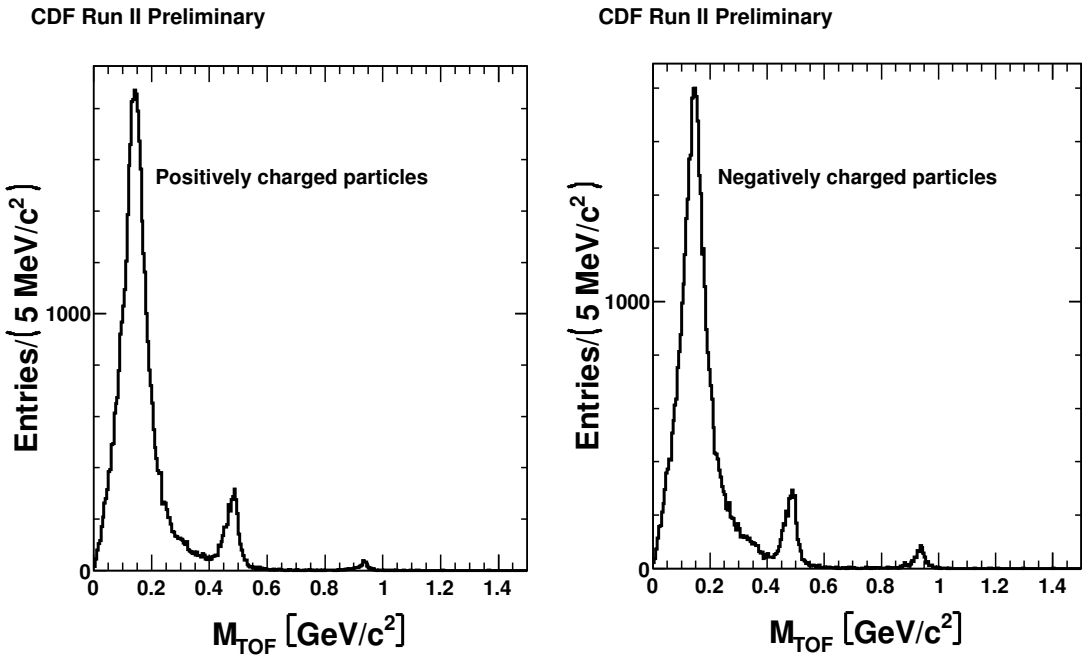

Figure 55: Mass calculated using Time of Flight for whole range of particle momentum for positively charged particles (left) and negatively charged particles (right).

$p\bar{p}$	0.4%
K^+K^-	2.1%
$\pi^+\pi^-$	86.2%
πK	9.7%

Table 10: Percentage contents of events with identified particular pair of particles using the TOF separation.

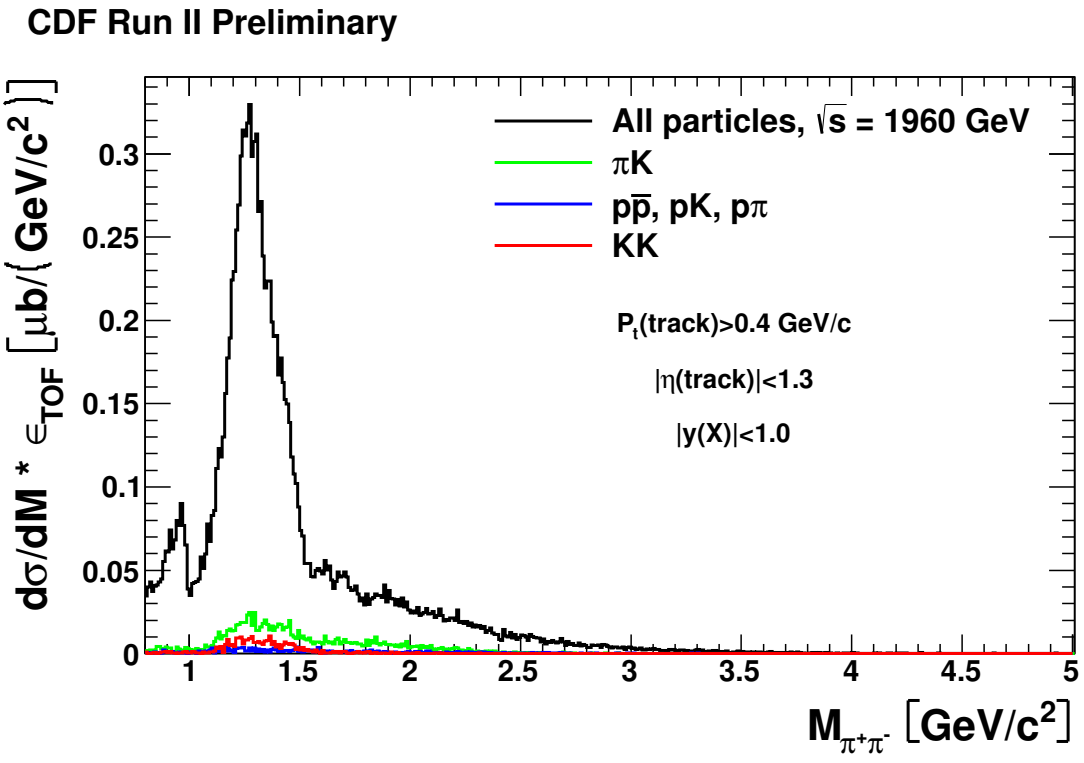

Figure 56: Invariant mass distribution for all selected particles assuming pions masses with contributions coming from non-$\pi\pi$ background identified with TOF method.

13.2 $K^0_S K^0_S$ events.

This section is a "place-holder" as the final acceptance and efficiency studies are ongoing. However it indicates that the K^+K^- "contamination" in the assumed $\pi^+\pi^-$ spectrum is less than a few percent.

We can measure exclusive $K^0_S + K^0_S \to 4\pi$ events, with four non-prompt tracks. The lifetime is given by $c\tau = 2.684$ cm, so the kaons in our momentum region ($\gamma = E/M \sim 1.3 - 5$) decay away from the beam line but in the inner part of the COT. We select events with four tracks, Q = 0, (with all exclusivity cuts) at 1960 GeV, selecting pairs with vertex displacement $L_{xy} > 0.5$ cm. A clean K^0 signal is seen with very little background. We then look for a second K^0_S; only about 3% of the events with one K^0_S have another one. (If the events are exclusive the other two tracks should be prompt $K^\pm\pi^\mp$; the subject of a different study.)

We find 578 events consistent with exclusive $K^0_S K^0_S \to (\pi^+\pi^-)(\pi^+\pi^-)$. The $K^0\bar{K^0}$ cross section is a factor of $\times 2$ higher to account for $K^0_L K^0_L$ ($K^0_S K^0_L$ being forbidden in D $\mathbb{P}$E), and we also have $\sigma(K^+K^-) = \sigma(K^0\bar{K^0})$. Applying the factors for the luminosity, exclusive efficiency and (preliminary) acceptance we estimate a cross section $d\sigma/dM(M(KK)) = 1.5{-}2.0$ GeV ~ 9.2 nb/GeV/c^2. Giving these, incorrectly, the pion mass they would populate the region $1.17 < M(\pi\pi) < 1.77$ GeV, with a (background) cross section $9.24/0.6 = 15.4$ nb/GeV. We can compare that with the cross section in Fig. 33, which averaged over that mass region about 18 nb/10 MeV = 1800 nb/GeV. This implies that the background under the $\pi^+\pi^-$ cross section in this region is $< 1\%$. In the region below $M(\pi\pi) = 1$ GeV/c^2 it appears to be even smaller. While this is very preliminary, we conclude from the few $K^0_S K^0_S$ events that K^+K^- is a very small background in the $\pi^+\pi^-$ spectra, corroborating the estimate from K^+K^-.

The mass dependence of both K^+K^- and $K^0_S K^0_S$ will be studied further, also at 900 GeV. We note (Table 5) the $f_2(1525)$ has a B.F. of nearly 90% to KK.

14 Summary and Conclusions

We have analysed a large sample of exclusive h^+h^- events at both $\sqrt{s} = 900$ and 1960 GeV (much larger than in other experiments with $\sqrt{s} > 30$ GeV), nearly all $\pi^+\pi^-$, that show several resonance features. We calculated the acceptance and studied the systematic uncertainties in the M, P_t plane.

We measured the backgrounds from K^+K^- and $p\bar{p}$ events using time of flight, and they are seen to be small (Fig. 56). The non-exclusive background is indicated both by (++) and (- -) pairs and the $K^\pm\pi^\mp$ events. Overall they are approximately 6% and 10% respectively, but the fraction is mass-dependent. We do not subtract them.

We have carried out a partial wave analysis and the data are consistent with only S-wave (J = 0) up to about 1.5 GeV/c^2, but must have (at 99% C.L.) higher waves above that mass. We cannot distinguish between J = 2 and J > 2 waves, mostly because of the limited angular coverage in the central region.

In parallel, and planned to be the subject of other notes, we are analysing the prompt-4-track data, as well as no-track data such as $\pi^0\pi^0$ and $\eta\eta \to 4\gamma$.

References

[1] S.Donnachie, G.Dosch, P.Landshoff and O.Nachtmann, Pomeron Physics and QCD, Cambridge University Press, 2002.

[2] V.Barone and E.Predazzi, High Energy Particke Diffraction, Springer, 2002.

[3] Quantum Chromodynamics and the Pomeron, J.R.Forshaw and D.A.Ross, Cambridge Lecure Notes in Physics, Cambridge University Press, 1997.

[4] M.G.Albrow, T.D.Coughlin, and J.R.Forshaw, Central exclusive particle production at hadron colliders, Prog.Part.Nucl.Phys. **65**, 149 (2010).

[5] T.Aaltonen *et al.*(CDF), Phys.Rev.Lett. **98**, 112001 (2007).

[6] T.Aaltonen *et al.* (CDF Collaboration), Phys.Rev.Lett. **102** 242001 (2009).

[7] T.Aaltonen *et al.* (CDF), Phys.Rev.Lett. **102** 222002 (2009).

[8] D.Acosta *et al.* (CDF), Phys.Rev.Lett. **93** 141601 (2004).

[9] T.Aaltonen *et al.* (CDF), Phys.Rev.D **77** 052004 (2008).

[10] T.Aaltonen *et al.* (CDF), Phys.Rev.Lett. **99**, 242002 (2007); T.Aaltonen *et al.* (CDF), Phys.Rev.Lett. **108**, 081801 (2012).

[11] J.L.Rosner, Phys. Rev. D **74** 076006 (2006).

[12] T.Akesson *et al.* (AFS Collaboration, C and jets), Phys.Lett. **128B**, 354 (1983).

[13] D.Acosta *et al.*, Estimation of CLC acceptance to inelastic $p\bar{p}$ interactions, CDF Note 6054.

[14] Nathan Goldschmidt, CDF NOTE 10650.

[15] G.Antchev *et al.*, (TOTEM Collabotration), arXiv:1204.5689, Prog.Theor.Phys.Suppl. **193** (2012) 180.

[16] C.Amsler, T.Gutsche, S.Spanier and N.A.Tornqvist, Note on Scalar Mesons in K.Nakamura *et al.*, (Particle Data Group), J. Phys. G. **37** 075021 (2010).

[17] D.Robson, Nucl. Phys. **B 130**, 328 (1977).

[18] T.Akesson *et al.* Phys. Lett. **133B** 268 (1983); T.Akesson *et al.*, Nucl. Phys. **B 264**, 154 (1986)

[19] K.L.Au, D.Morgan and M.R.Pennington, Phys. Rev. D **35**, 1633 (1987); K.L.Au, D.Morgan and M.R.Pennington, DTP-86/8, Proc. 21st Rencontre de Moriond (1986).

[20] R.Carosi *et al.* (CDF) Particle identification by combining TOF and dE/dx information, CDF/PHYS/CDF/CDFR/7488 (2005).

[21] O.V.Teryaev, R.S.Pasechnik, and A.Szczurek, Central exclusive χ_c production, Proc. 13th Int. Conf. Blois, CERN (2009)

[22] D.Moran (LHCb) Ph.D. Thesis (2011). Central exclusive production with dimuon final states at LHCb.

[23] M.Jacob and G.C.Witt, Annal. Phys. **7** (1959) 404.